Article

Geminal-atom catalysis for cross-coupling

https://doi.org/10.1038/s41586-023-06529-z

Received: 3 May 2022

Accepted: 10 August 2023

Published online: 20 September 2023

Check for updates

Xiao Hai[1,12], Yang Zheng[1,12], Qi Yu[2,3,12], Na Guo[4,5,12], Shibo Xi[6]✉, Xiaoxu Zhao[7], Sharon Mitchell[8], Xiaohua Luo[1], Victor Tulus[8], Mu Wang[1], Xiaoyu Sheng[1], Longbin Ren[1], Xiangdong Long[1], Jing Li[1], Peng He[1], Huihui Lin[1], Yige Cui[1], Xinnan Peng[1], Jiwei Shi[1], Jie Wu[1], Chun Zhang[1,4,5], Ruqiang Zou[7], Gonzalo Guillén-Gosálbez[8], Javier Pérez-Ramírez[8]✉, Ming Joo Koh[1]✉, Ye Zhu[1]✉, Jun Li[9,10,11]✉ & Jiong Lu[1]✉

Single-atom catalysts (SACs) have well-defined active sites, making them of potential interest for organic synthesis[1–4]. However, the architecture of these mononuclear metal species stabilized on solid supports may not be optimal for catalysing complex molecular transformations owing to restricted spatial environment and electronic quantum states[5,6]. Here we report a class of heterogeneous geminal-atom catalysts (GACs), which pair single-atom sites in specific coordination and spatial proximity. Regularly separated nitrogen anchoring groups with delocalized π-bonding nature in a polymeric carbon nitride (PCN) host[7] permit the coordination of Cu geminal sites with a ground-state separation of about 4 Å at high metal density[8]. The adaptable coordination of individual Cu sites in GACs enables a cooperative bridge-coupling pathway through dynamic Cu–Cu bonding for diverse C–X (X = C, N, O, S) cross-couplings with a low activation barrier. In situ characterization and quantum-theoretical studies show that such a dynamic process for cross-coupling is triggered by the adsorption of two different reactants at geminal metal sites, rendering homo-coupling unfeasible. These intrinsic advantages of GACs enable the assembly of heterocycles with several coordination sites, sterically congested scaffolds and pharmaceuticals with highly specific and stable activity. Scale-up experiments and translation to continuous flow suggest broad applicability for the manufacturing of fine chemicals.

Transition-metal-catalysed cross-coupling reactions, which are critical for developing molecular complexity in organic syntheses, typically exploit homogeneous organometallic complexes[9–11]. Despite their unparalleled synthetic capability, concerns arising from using homogeneous catalysts include their potentially high production costs, the environmental impact associated with challenges in product separation and purification, and catalyst recycling[12,13]. The development of heterogeneously catalysed processes is highly attractive for large-scale production to facilitate catalyst separation, recovery and reuse, and improve adaptability for continuous-flow synthesis[4,14,15]. These potential advantages have provoked extensive studies of immobilized organometallic complexes and nanostructured metal catalysts[16]. Although some have been successfully implemented industrially, their applicability in cross-coupling reactions remains limited, primarily owing to poor control of active-site structures or weak interactions with supports[17].

Heterogeneous SACs, which integrate well-defined mononuclear metal sites, have sparked interest for their potential to overcome the shortcomings of previously developed catalytic solids[1,2,18,19]. The carrier design must ensure the stability of metal centres while permitting structural flexibility to fulfil the catalytic cycle and achieve enzyme-like specific activity[20]. Nonetheless, the chemical bonding between the metal centre and the carrier required to prevent metal detachment or aggregation typically leads to restricted spatial environment (for example, high coordination numbers), limiting its capacity to activate complicated or multiple substrates simultaneously[21,22]. These seemingly conflicting requirements have prompted debate over whether mononuclear metal sites provide the optimal architecture for complex molecular transformations. Some researchers have postulated that tailored multinuclear sites may be more efficient, but controlled synthetic routes for other low-nuclearity catalysts remain limited[3]. An alternative approach would be to exploit cooperativity between metal centres in SACs by controlling their spatial proximity[23] (Supplementary Fig. 1).

Here we develop a new class of heterogeneous GACs consisting of pairs of low-valence metal centres with a regular ground-state separation and suitable coordination dynamics to enable site cooperativity. The concept is demonstrated for copper atoms anchored on a nanocrystalline PCN carrier, which defines the proximity of metal sites of about 4 Å and enables their adaptive coordination during

[1]Department of Chemistry, National University of Singapore, Singapore, Singapore. [2]School of Materials Science and Engineering, Shaanxi University of Technology, Hanzhong, China. [3]Shaanxi Key Laboratory of Catalysis, Shaanxi University of Technology, Hanzhong, China. [4]National University of Singapore (Chongqing) Research Institute, Chongqing, China. [5]Department of Physics, National University of Singapore, Singapore, Singapore. [6]Institute of Sustainability for Chemicals, Energy and Environment (ISCE2), Agency for Science, Technology and Research (A*STAR), Singapore, Singapore. [7]School of Materials Science and Engineering, Peking University, Beijing, China. [8]Institute for Chemical and Bioengineering, Department of Chemistry and Applied Biosciences, ETH Zurich, Zürich, Switzerland. [9]Department of Chemistry and Engineering Research Center of Advanced Rare-Earth Materials of Ministry of Education, Tsinghua University, Beijing, China. [10]Department of Chemistry, Southern University of Science and Technology, Shenzhen, China. [11]Guangdong Provincial Key Laboratory of Catalytic Chemistry, Southern University of Science and Technology, Shenzhen, China. [12]These authors contributed equally: Xiao Hai, Yang Zheng, Qi Yu, Na Guo. ✉e-mail: xi_shibo@partner.nus.edu.sg; jpr@chem.ethz.ch; chmkmj@nus.edu.sg; chmzhu@nus.edu.sg; junli@tsinghua.edu.cn; chmluj@nus.edu.sg

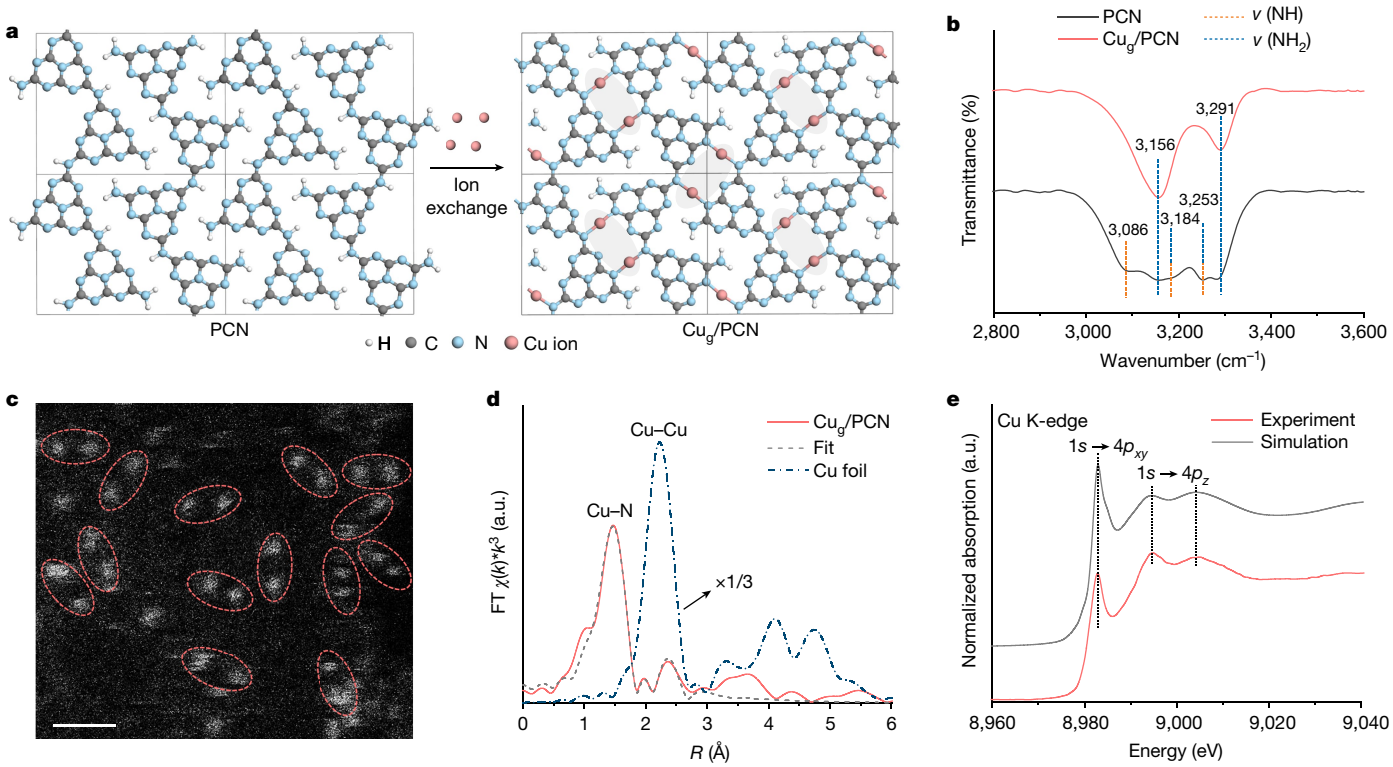

Fig. 1 | Synthesis and characterization of Cu$_g$/PCN. a, Strategy for the preparation of Cu$_g$/PCN GACs based on the periodic crystal structure of the host. **b**, FTIR spectra of PCN and Cu$_g$/PCN. **c**, Atomic-resolution ADF-STEM image (geminal Cu structures are circled). Scale bar, 0.5 nm. **d**, k^3-weighted Cu K-edge Fourier-transformed (FT) EXAFS spectra of Cu$_g$/PCN and Cu foil as reference. **e**, The experimental high-resolution XANES spectrum compared with the calculated XANES data of optimized DFT-modelled structure of Cu$_g$/PCN. a.u., arbitrary units.

the reaction. Catalytic evaluation in a broad range of cross-coupling reactions, including azide–alkyne cycloaddition, carbon–carbon and carbon–heteroatom bond formation, demonstrates the superior performance of GACs compared with conventional SACs with a similar metal density based on a nitrogen-doped carbon host. The results show that GACs overcome the sluggish oxidative addition in copper-catalysed cross-coupling reactions, which has traditionally limited the scope compared with palladium catalysts, despite the lower cost and environmental footprint of copper. Detailed structural and mechanism analysis confirms the cooperativity of metal centres in the geminal sites, enabling the efficient activation of substrates through a dynamic bridge-coupling mechanism. Further demonstration in the production of biorelevant pharmaceuticals and translation to continuous flow illustrate the broad synthetic capability of GACs. Quantification of the environmental benefits of the present GACs route compared with conventional homogeneous synthesis by means of an ex ante life-cycle assessment (LCA) highlights a reduced footprint in four well-established metrics.

Synthesis and characterization of GACs

A stepwise ion exchange and ligand removal strategy was devised for the synthesis of low-coordinate geminal metal atoms exploiting the abundant and periodic presence of N-H functional groups as metal coordination sites in PCN[24,25] (Fig. 1a and Supplementary Fig. 2). On introduction, Cu single atoms replace H atoms, as confirmed by the almost completely reduced intensity of N-H-group-related vibration bands of PCN (Fig. 1b), and are further stabilized by the opposite N atoms[26]. Annular dark-field scanning transmission electron microscopy (ADF-STEM; Fig. 1c) acquired over ultrahigh-density Cu$_g$/PCN (18.3 wt% Cu) shows a high concentration of metal atoms, which tend to form regularly spaced pairs (termed geminal Cu) with an average Cu–Cu distance of approximately 0.4 nm. Such a geminal Cu pair anchored in a PCN chain is also captured by in situ scanning tunnelling microscopy (STM) characterization (Extended Data Fig. 1). Elemental mapping using energy-dispersive X-ray spectroscopy and powder X-ray diffraction (XRD) measurements also confirm the uniform metal dispersion and the absence of nanoparticles or clusters in Cu$_g$/PCN (Extended Data Fig. 2). Consistently, the Fourier-transformed extended X-ray absorption fine structure (EXAFS; Fig. 1d and Supplementary Table 1) spectrum shows a dominant feature centred at 1.5 Å and a weak peak at around 2.2 Å, corresponding to the first shell Cu–N and the second shell Cu–C interatomic distance, respectively. A prominent shoulder feature around 8,983 eV in the Cu K-edge X-ray absorption near edge structure (XANES) can be assigned to the $1s \rightarrow 4p_{xy}$ transition, indicative of a diagonal coordinated Cu (ref. 27). To confirm the atomic structure of the Cu sites, first-principles calculations based on density functional theory (DFT) were conducted to identify possible models and simulate their corresponding XANES spectra. Among all the proposed structures[7] (Extended Data Fig. 3), the one consisting of heptazine chains shows the best agreement with the experimental Cu K-edge XANES spectrum (Fig. 1e). Such a diagonally coordinated N–Cu–N structure endows a Cu valence state of +1 and this monovalent Cu(I) state is further confirmed by X-ray photoelectron spectroscopy and electron paramagnetic resonance (EPR) spectroscopy (Extended Data Fig. 3).

Performance in cross-coupling reactions

To assess the reaction scope of the Cu$_g$/PCN catalyst, various (hetero) aryl halides with different electronic and/or steric attributes were examined under ligand-free conditions (Supplementary Table 2 and Supplementary Fig. 3). The results demonstrate that Cu$_g$/PCN is an efficient heterogeneous catalyst for general cross-coupling reactions,

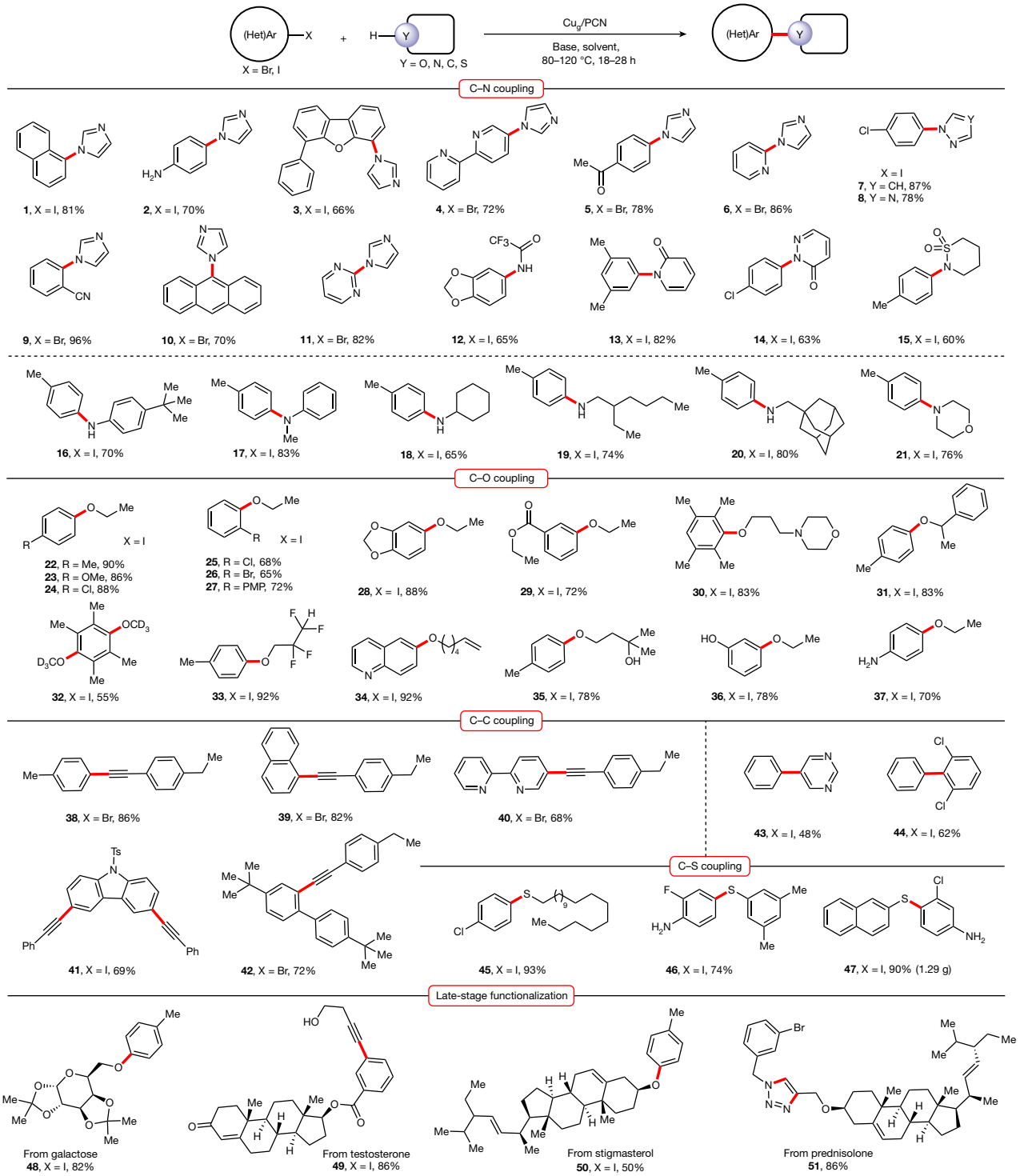

Fig. 2 | Substrate scope of Cu$_g$/PCN-catalysed cross-couplings. Product yields obtained in Cu$_g$/PCN-catalysed C–N, C–O, C–C and C–S bond formations and late-stage modification of biorelevant molecules with a broad scope of (hetero)aryl halides. Reaction conditions (1.4 mol% Cu): C–N bond formation, aryl halide (0.2 mmol), nitrogen-based nucleophile (0.24 mmol for N-heterocyclic compounds, 0.3 mmol for primary and secondary amines), 0.4 mmol base (K_3PO_4 for N-heterocyclic compounds, NaOH for primary and secondary amines), anhydrous DMSO (1.0 ml), 110 °C 28 h; C–O bond formation, aryl iodide (0.2 mmol), alcohol (0.4 mmol), KO*t*Bu (0.3 mmol), anhydrous dioxane (2.0 ml), 80 °C 18 h; C–C bond formation, aryl halide (0.2 mmol), alkyne (0.3 mmol, for di-halide aromatic ring, 0.6 mmol), $Cs(OH)_2.H_2O$ (0.3 mmol, for di-halide aromatic ring, 0.6 mmol) and anhydrous DMSO (1.0 ml), 110 °C 28 h; C–S bond formation, aryl halide (0.2 mmol), mercaptan/thiophenol (0.3 mmol), NaO*t*Bu (0.30 mmol) and anhydrous dioxane (2.0 ml), 80 °C 18 h.

transforming diverse reactants to targeted molecules with high selectivity and yields (Fig. 2 and Extended Data Fig. 4). Aryl and heteroaryl iodides and bromides are excellent coupling partners, affording a wide spectrum of products in good to excellent yields (**1**–**82**). Electron-donating, electron-withdrawing, functional substituents (for example, hydroxyl, amino, halide, ester, ketone, nitrile, alkene, alkyne) and heterocycles are well tolerated, providing great flexibility for further synthetic manipulations. In particular, nitrogen heterocycles (**1**–**11**, **52**–**61**), amides (**12**–**14**, **62**), sulfonamide (**15**), aryl amines (**16**,**17**,**63**–**69**) and alkylamines (**18**–**21**,**70**) all participate in C–N coupling,

yielding diverse functionalized nitrogen-containing compounds. Fluorinated alcohols (**33**, **82**) and deuterated methanol (**32**, **80**, **81**) are effective substrates for C–O coupling. Synthetically useful C–C coupling using terminal alkynes (**38**–**42**) or electron-deficient (hetero) arenes (**43**, **44**) can also be achieved. The GACs system outperforms Cu nanocatalysts and benchmarked homogeneous cuprous iodide at the same molar equivalent of copper (Supplementary Table 3). Furthermore, Cu_g/PCN demonstrated excellent performance (**83**–**90**, 88–94% yield) for azide–alkyne cycloaddition, a reaction known to involve two metal centres[28]. The Cu_g/PCN-catalysed cross-coupling is scalable: production of *p*-ethoxytoluene (**22**) was successfully executed on the 26-g scale, affording the C–O coupling product in 87% isolated yield (Supplementary Fig. 4).

The compatibility of the GAC system was further tested on biorelevant molecules. Representative examples involving the cross-coupling of DL-menthol (**94**, **95**), stigmasterol (**50**), DL-isoborneol (**96**), 1,2,3,4-diacetone galactose (**48**) and the derivatives of testosterone (**49**) and prednisolone (**51**) (Fig. 2 and Extended Data Fig. 5), as well as the large-scale synthesis of drug-like *p*-arylthio aniline (**47**, 1.2 g), smoothly proceeded to deliver the corresponding products, highlighting the applicability for late-stage modification of complex molecules of the Cu_g/PCN catalyst. Starting from commercially available substrates, batch synthesis of selected pharmaceutically active compounds (**91**–**93**) was also successfully accomplished (Extended Data Fig. 5).

Reaction mechanism

To confirm the unique site cooperativity in the GACs, a series of Cu SACs (Cu_1/PCN) was prepared with Cu contents ranging from 0.2 to 18.3 wt%, for which the ratio of monomeric Cu(I) to geminal Cu(I)…Cu(I) sites is expected to decrease on increasing the Cu content in the sample (Supplementary Fig. 5). Meanwhile, detailed characterization (Extended Data Fig. 6) and quantum-theoretical studies based on DFT calculations (Extended Data Fig. 7) show the identical chemical state of each Cu regardless of the metal content. The catalytic performance of Cu_1/PCN catalysts with different Cu contents for C–N, C–O cross-coupling and azide–alkyne cycloaddition were evaluated using the same amount of Cu (2 mol%), respectively (Supplementary Table 4). Similar trends were observed in all cases: the product yields correlate with the metal content increasing from zero in the sample containing 0.2 wt% Cu, in which all the Cu(I) sites are isolated monomers, to around 90% over the catalyst with the highest content of geminal sites. This control experiment reveals the inability of a monomer Cu(I) to trigger the coupling reaction because of the high energy barrier for oxidation of low-valent copper to a trivalent Cu(III) intermediate, highlighting the necessity of a geminal Cu(I)…Cu(I) structure. The low valence state of the metal centre endowed by the diagonally coordinated N–Cu–N configuration also plays an important role in the activation of reactants. This is by stark contrast to zero activity observed over ultrahigh-density divalent single-atom Cu(II) on nitrogen-doped carbon for the C–O coupling reaction, even if the catalyst contains an abundance of adjacent CuN_4 sites[8] (Supplementary Fig. 6).

Given the well-documented difficulty of oxidative addition on Cu, we performed quantum-theoretical investigations (periodic and cluster models; Supplementary Fig. 7) to explore the coupling of 4-iodobenzene with methanol to gain molecular-level understanding of the cross-bond formation mediated by Cu_g/PCN. Initiation is induced by the separate adsorption of (hetero)aryl halide (4-iodobenzene) and the partner nucleophilic reactant (methanol) over each Cu(I) atom of the geminal site. Comprehensive theoretical calculations on the plausible mechanisms strongly support the preference of a direct coupling pathway, in which a dynamically formed Cu_2 dimer with direct Cu–Cu bonding facilitates C–O bond formation through oxidation addition and subsequent elimination to yield $C_6H_5OCH_3$ (Fig. 3 and Supplementary Fig. 8). The unique heptazine chain structure allows for the adaptive migration of the geminal Cu (named Cu_A and Cu_B) towards each other on the adsorption of reactants (Fig. 3a and Supplementary Table 5), bringing the two reactants ($*C_6H_5$ and $*OCH_3$) close enough for the direct cross-bond formation. The system naturally returns to the original static state with unbonded Cu(I)…Cu (I) sites after desorption of the product (Fig. 3c and Supplementary Video 1). Such a dynamic reconfiguration of geminal Cu sites during reaction is expected to be energetically costly, which can be largely offset by electronic energy gain through Cu–Cu bonding orbital interaction. Owing to quantum primogenic effect[29], the atomic radial orbital extension of Cu 4*s* (about 2.2 Å) is much larger than Cu 3*d* (about 1.3 Å) in the radial probability distribution (Supplementary Fig. 9), so that the Cu_2 dimer formation is energetically compensated through Cu–Cu 4*s*–4*s* bonding[30]. Indeed, chemical-bonding analysis shows that the 4*s*–4*s* orbital interaction between the geminal Cu(II) will cause the system to undergo a potential-energy-surface crossing from $Cu^{II}(d^9s^0)$…$Cu^{II}(d^9s^0)$ triplet to $Cu^{II}(d^8s^1)$–$Cu^{II}(d^8s^1)$ singlet states when the direct 4*s*–4*s* σ-bond is formed (Fig. 3b). Furthermore, DFT calculations indicate that the alternative pathway involving the simultaneous oxidative addition of two reactants over a single copper has a much higher energy barrier (>2.45 eV), thus ruling out the possibility of a cross-coupling reaction occurring over an isolated monoatomic copper (Supplementary Fig. 10).

Apart from this, our theoretical calculations also show that the adsorption state of individual Cu sites in GACs exhibits negligible mutual influence, distinct from the conventional static dual-atom or bimetallic complex catalysts with a strong direct or indirect metal–metal interaction[31,32]. For example, the calculated adsorption energies for the individual $*C_6H_5$ and $*OCH_3$ on the Cu atoms amount to −0.90 eV and −1.04 eV, respectively. In the scenario where $*OCH_3$ is pre-adsorbed on the Cu_A site, the resulting adsorption energy of $*C_6H_5$ on the Cu_B site is determined as −0.94 eV. Similarly, upon the pre-adsorption of $*C_6H_5$ on the Cu_A site, the calculated adsorption energy of $*OCH_3$ on the Cu_B site is −1.08 eV. Notably, the co-adsorption process can occur only under the combination of 4-iodobenzene with methanol (neither two 4-iodobenzene nor two methanol molecules), which can explain why only cross-coupling products were obtained instead of homo-coupling products in the C–O coupling reaction (Supplementary Figs. 11 and 12). The adsorption of 4-iodobenzene and methanol on Cu sites caused the crucial Cu(I)-to-Cu(II) valence-state conversion, which is directly evidenced by EPR spectroscopic measurements (Supplementary Fig. 13), in which the EPR-silent $Cu(I,d^{10}s^0)$ in Cu_g/PCN is oxidized to EPR-sensitive $Cu(II,d^9s^0)$. Further analysis of the calculated projected density of states (PDOS) (Supplementary Fig. 14) and variation in the Bader charges (Supplementary Table 6) and spin density population of Cu in Cu_g/PCN confirms that the valence state of Cu after adsorbing $*C_6H_5$ or $*CH_3O$ becomes Cu(II), consistent with the EPR result. Also, the calculated energy profile reveals the activation of 4-iodobenzene with an activation barrier larger than 0.98 eV, represents the rate-determining step for C–O coupling, consistent with the experimental results (Supplementary Fig. 15). The proposed theoretical framework was further validated through in situ XAFS and EPR experiments (Extended Data Fig. 8), which efficiently track the chemical state and local bonding environment evolution of Cu species during the whole reaction cycle.

Distinct advantages of GACs

The versatility of Cu_g/PCN was further showcased by evaluating the catalyst in various synthetic scenarios (Fig. 4). In the N-arylation of imidazoles (**97**, **71**, **72**), Cu_g/PCN exhibited enhanced regioselectivity compared with the benchmark homogeneous 1,10-phenanthroline-ligated copper catalyst[33], suggesting a notable advantage of GACs in facilitating the formation of multifunctional heterocycles that are common in natural products and pharmaceuticals (Fig. 4a, Extended Data Fig. 4 and Supplementary Fig. 16). Encouragingly, the performance of

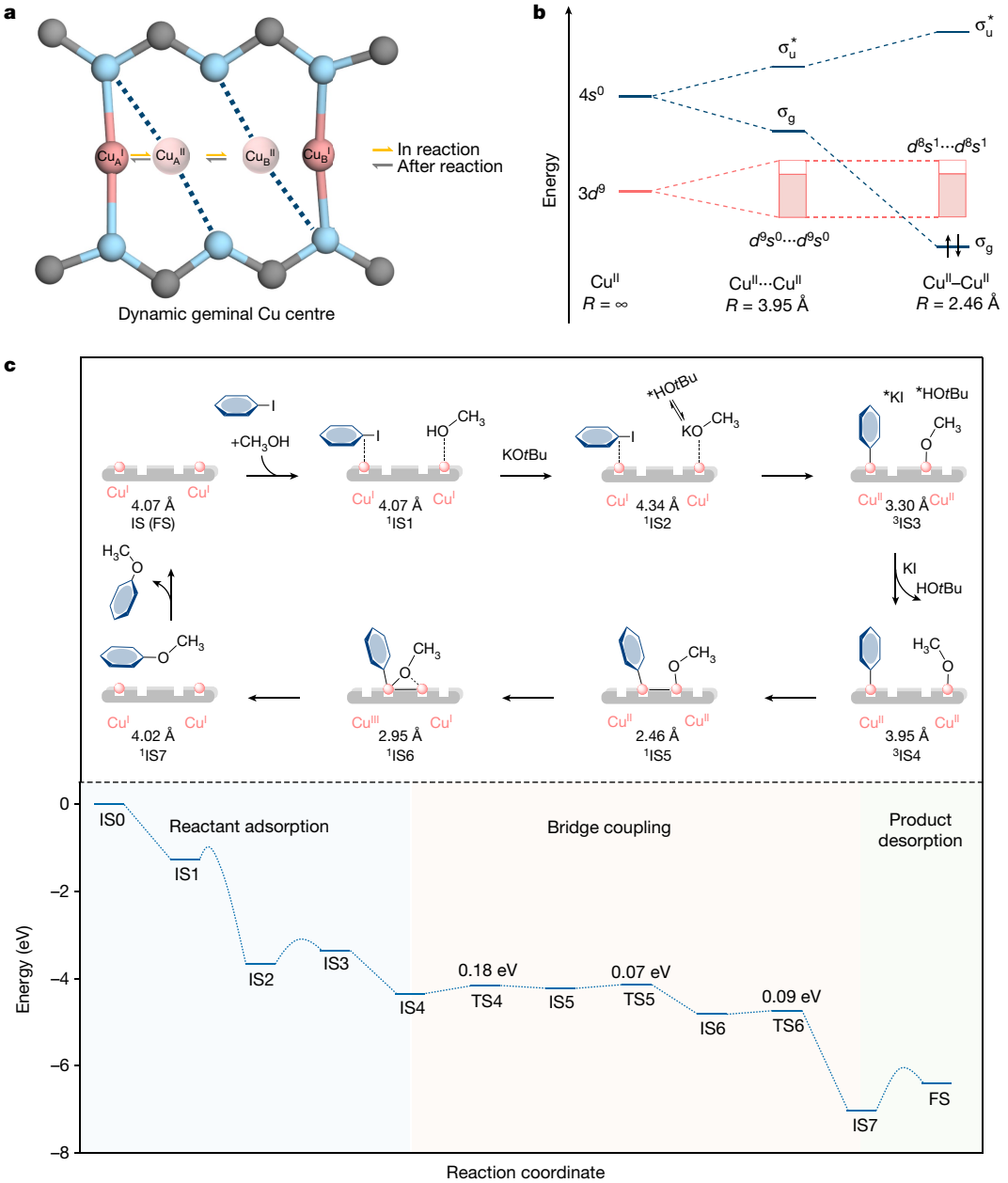

Fig. 3 | Proposed catalytic mechanism of C–O coupling over Cu_g/PCN. **a**, Schematic illustration of the dynamic coordination of geminal Cu active centres. **b**, The energy levels of Cu(II)…Cu(II) interaction with increasing proximity from distance (∞) to 2.46 Å. **c**, The proposed reaction mechanism and the calculated energy profiles for C–O bond formation mediated by Cu_g/PCN. The spin state, valence state and Cu…Cu distance are marked in the figure.

Cu_g/PCN in the C–N coupling reaction was not compromised by an exogenous equivalent of terpyridine (Fig. 4b), highlighting the tolerance of the catalyst to multi-coordinating entities. Moreover, the Cu_g/PCN catalyst addressed practical shortcomings of reported synthetic routes to synthetically challenging pharmaceuticals. For example, a more readily available bromide substrate (this work, 1.4 mol% Cu catalyst, 62% yield) was successfully used in C–N coupling (previously iodide substrate, 3 equivalents Cu powder, 53% yield), improving the overall synthesis of dutasteride[34] (**98**), a synthetic 4-azasteroid derivative used primarily to treat prostate disease (Fig. 4c). Similarly, a more efficient and cost-effective Ullmann coupling (this work, 1.4 mol% Cu catalyst, 65% yield) using a bromide substrate was designed as an alternative for the previously reported Chan–Lam coupling involving a more expensive boronic acid (2 equivalents Cu complex, 38% yield) for the synthesis of a precursor of xanthine derivatives[35] (**99**), which are used as kinase inhibitors (Fig. 4d). By using catalytic amounts of recyclable Cu_g/PCN, stoichiometric amounts of copper waste can be avoided, which will otherwise lead to product contamination and other environmental issues[14]. Furthermore, Cu_g/PCN demonstrated its capability in promoting cross-coupling reactions involving sterically demanding substrates, enabling the synthesis of the precursor of chiral spiro Cp ligands[36] (**100**), which are important in asymmetric catalysis[37]. Through this direct cross-coupling with Cu_g/PCN, the precursor can be secured in a single step in 52% yield, compared with the previous route that required three steps to deliver **100** in 22% overall yield because direct cross-coupling with isopropanol was inefficient in the presence of the homogeneous copper-based catalyst (Fig. 4e). These examples underline the power of Cu_g/PCN in overcoming challenges in organic synthesis, making them attractive candidates for practical adoption in fine-chemical production.

A further key advantage of using heterogeneous catalysts lies in their recoverability and reusability. Cu_g/PCN demonstrated excellent

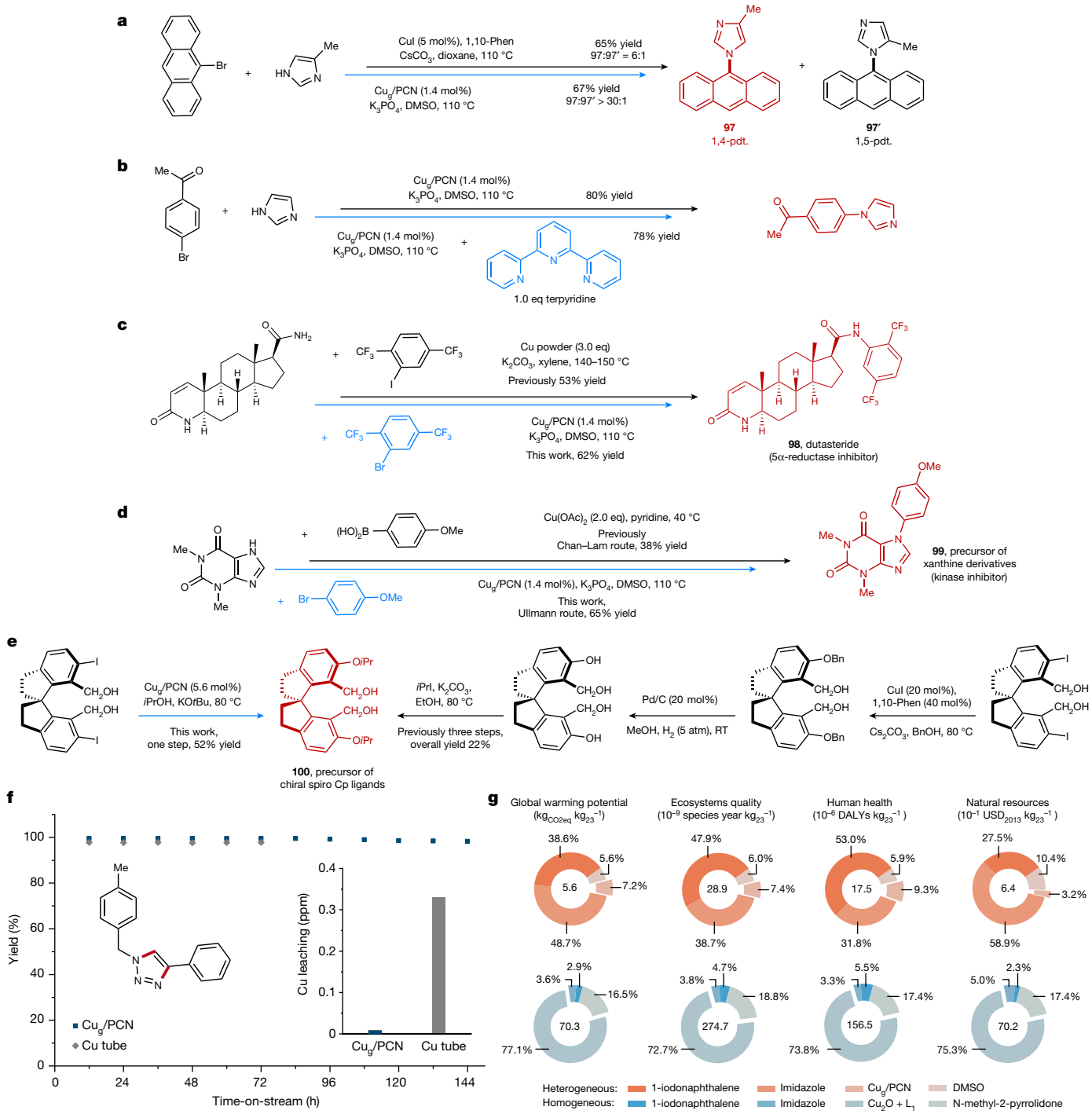

Fig. 4 | Advantages of geminal-atom catalysis for organic synthesis. **a**, Regioselectivity differences in the synthesis of 1,4-substituted imidazoles with different copper catalysts. **b**, C–N cross-coupling reaction catalysed by Cu_g/PCN in the presence of an equivalent of terpyridine. **c**, Comparison between the previous route and the Cu_g/PCN approach in the synthesis of dutasteride. **d**, Comparison between the previous Chan–Lam route and the newly designed Ullmann approach in the synthesis of a xanthine precursor. **e**, Comparison between the previous route and the Cu_g/PCN approach in the synthesis of a chiral spiro Cp ligand precursor. **f**, Continuous-flow synthesis of 1-(4-methylbenzyl)-4-phenyl-1*H*-1,2,3-triazole as a function of time-on-stream over Cu_g/PCN and Cu tube, respectively. The inset shows the measured concentration of Cu ions leached into the solution at the end of each reaction. **g**, LCA impact assessment of heterogeneously and homogeneously catalysed C–N coupling. Impact contributions are based on the performance of Cu_g/PCN or $Cu_2O + L_1$ (L_1 = 4,7-dimethoxy-1,10-phenanthroline) in the synthesis of 1-(naphthalen-1-yl)-1*H*-imidazole through the coupling of imidazole and 1-iodonaphthalene. DALYs, disability-adjusted life years; RT, room temperature; USD, US dollars.

durability and recyclability in the C–O coupling reaction as shown in Extended Data Fig. 9, with no appreciable conversion and selectivity decrease over nine consecutive runs. Consistently, inductively coupled plasma atomic emission spectroscopy analysis of the used catalyst confirms the virtually identical amounts of Cu to the fresh Cu_g/PCN, accompanied by the absence of any detectable Cu ions in solution. The ADF-STEM image acquired over the used Cu_g/PCN catalyst showed a high density of atoms with no visible nanoparticle

aggregation, suggesting that the atomic dispersion of copper species was preserved after the catalytic reaction (Supplementary Fig. 17). Fourier transform infrared (FTIR), XRD, X-ray photoelectron spectroscopy (XPS), Cu K-edge XANES and EXAFS analysis also revealed the identical atomic structures of Cu in the used catalyst to the fresh Cu_g/PCN (Extended Data Fig. 9). Also, the coupling of 4-iodotoluene with ethanol occurred in the presence of 0.01 mol% Cu (Cu_g/PCN) to give the desired product in 80% yield, corresponding to a turnover number of 8,000, which is almost two orders of magnitude higher than the homogeneous copper-catalysed cross-coupling of an aryl halide with aliphatic alcohol[38]. It is worth noting that the obtained turnover number value is probably underestimated owing to the active-site blockage by the deposition of insoluble salts (Supplementary Fig. 18). Furthermore, motivated by substantial developments to improve synthetic efficiency and the intensification of chemical processes, we translated the batch synthesis over Cu_g/PCN to a continuous-flow protocol, which has distinct advantages in terms of automation and process optimization[39] (Supplementary Fig. 19). Evaluation in a custom-made packed-bed reactor evidenced a stable gradient production of ethoxybenzene under varying flow rates (Supplementary Fig. 20) and a constant production of 1-(4-methylbenzyl)-4-phenyl-1*H*-1,2,3-triazole on stream for more than 144 h with no obvious variation in selectivity or yield (Fig. 4f), as well as the negligible leaching of Cu ions into solution compared with commercially available copper tube flow reactors (Fig. 4f inset).

Finally, we have quantified the environmental benefits of the geminal-atom-catalysed route compared with conventional homogeneous synthesis through LCA. This analysis, which provided a detailed cradle-to-gate evaluation of the impacts of all the reaction components, revealed substantially reduced environmental footprint of the heterogeneous catalyst and highlighted the dominant contribution of the ligand in the homogeneous system (Fig. 4g and Supplementary Figs. 21 and 22). Moreover, sensitivity analysis on the LCA results shows that it would be difficult to find a homogenous counterpart that shows substantially better environmental performance, as contributions of the catalyst and solvent to the total impact in the heterogeneous system are already low (Supplementary Fig. 23).

Online content

Any methods, additional references, Nature Portfolio reporting summaries, source data, extended data, supplementary information, acknowledgements, peer review information; details of author contributions and competing interests; and statements of data and code availability are available at https://doi.org/10.1038/s41586-023-06529-z.

1. Cui, X., Li, W., Ryabchuk, P., Junge, K. & Beller, M. Bridging homogeneous and heterogeneous catalysis by heterogeneous single-metal-site catalysts. *Nat. Catal.* **1**, 385–397 (2018).
2. Li, W.-H., Yang, J., Wang, D. & Li, Y. Striding the threshold of an atom era of organic synthesis by single-atom catalysis. *Chem* **8**, 119–140 (2022).
3. Yan, H., Su, C., He, J. & Chen, W. Single-atom catalysts and their applications in organic chemistry. *J. Mater. Chem. A* **6**, 8793–8814 (2018).
4. Giannakakis, G., Mitchell, S. & Pérez-Ramírez, J. Single-atom heterogeneous catalysts for sustainable organic synthesis. *Trends Chem.* **4**, 264–276 (2022).
5. Lang, R. et al. Single-atom catalysts based on the metal–oxide interaction. *Chem. Rev.* **120**, 11986–12043 (2020).
6. Shan, J. et al. Metal-metal interactions in correlated single-atom catalysts. *Sci. Adv.* **8**, eabo0762 (2022).
7. Kessler, F. K. et al. Functional carbon nitride materials—design strategies for electrochemical devices. *Nat. Rev. Mater.* **2**, 17030 (2017).
8. Hai, X. et al. Scalable two-step annealing method for preparing ultra-high-density single-atom catalyst libraries. *Nat. Nanotechnol.* **17**, 174–181 (2022).
9. Bolm, C. & Beller, M. *Transition Metals for Organic Synthesis* Vol. 1 (Wiley, 2004).
10. Brandsma, L., Vasilevsky, S. F. & Verkruijsse, H. D. *Application of Transition Metal Catalysts in Organic Synthesis* (Springer, 2012).
11. De Meijere, A., Bräse, S. & Oestreich, M. *Metal-Catalyzed Cross-Coupling Reactions and More* Vol. 1 (Wiley, 2014).
12. Sheldon, R. A. & Van Bekkum, H. *Fine Chemicals Through Heterogeneous Catalysis* (Wiley, 2008).
13. Biffis, A., Centomo, P., Del Zotto, A. & Zecca, M. Pd metal catalysts for cross-couplings and related reactions in the 21st century: a critical review. *Chem. Rev.* **118**, 2249–2295 (2018).
14. Vásquez-Céspedes, S., Betori, R. C., Cismesia, M. A., Kirsch, J. K. & Yang, Q. Heterogeneous catalysis for cross-coupling reactions: an underutilized powerful and sustainable tool in the fine chemical industry? *Org. Process Res. Dev.* **25**, 740–753 (2021).
15. Tsubogo, T., Oyamada, H. & Kobayashi, S. Multistep continuous-flow synthesis of (R)- and (S)-rolipram using heterogeneous catalysts. *Nature* **520**, 329–332 (2015).
16. Benaglia, M. & Puglisi, A. *Catalyst Immobilization: Methods and Applications* (Wiley, 2019).
17. Kalz, K. F. et al. Future challenges in heterogeneous catalysis: understanding catalysts under dynamic reaction conditions. *ChemCatChem* **9**, 17–29 (2017).
18. Qiao, B. et al. Single-atom catalysis of CO oxidation using Pt_1/FeO_x. *Nat. Chem.* **3**, 634–641 (2011).
19. Wang, A., Li, J. & Zhang, T. Heterogeneous single-atom catalysis. *Nat. Rev. Chem.* **2**, 65–81 (2018).
20. Chen, Z. et al. A heterogeneous single-atom palladium catalyst surpassing homogeneous systems for Suzuki coupling. *Nat. Nanotechnol.* **13**, 702–707 (2018).
21. Kaiser, S. K., Chen, Z., Faust Akl, D., Mitchell, S. & Pérez-Ramírez, J. Single-atom catalysts across the periodic table. *Chem. Rev.* **120**, 11703–11809 (2020).
22. Li, Z. et al. Well-defined materials for heterogeneous catalysis: from nanoparticles to isolated single-atom sites. *Chem. Rev.* **120**, 623–682 (2019).
23. Regalbuto, J. R. & Datye, A. K. All the lonely atoms, where do they all belong? *Nat. Nanotechnol.* **17**, 110–111 (2022).
24. Tyborski, T. et al. Crystal structure of polymeric carbon nitride and the determination of its process-temperature-induced modifications. *J. Phys. Condens. Matter* **25**, 395402 (2013).
25. Fina, F., Callear, S. K., Carins, G. M. & Irvine, J. T. Structural investigation of graphitic carbon nitride via XRD and neutron diffraction. *Chem. Mater.* **27**, 2612–2618 (2015).
26. Stuart, B. H. *Infrared Spectroscopy: Fundamentals and Applications* (Wiley, 2004).
27. Sendzik, M., Pushie, M. J., Stefaniak, E. & Haas, K. L. Structure and affinity of Cu(I) bound to human serum albumin. *Inorg. Chem.* **56**, 15057–15065 (2017).
28. Worrell, B., Malik, J. & Fokin, V. V. Direct evidence of a dinuclear copper intermediate in Cu(I)-catalyzed azide-alkyne cycloadditions. *Science* **340**, 457–460 (2013).
29. Tang, Y., Wang, Y.-G. & Li, J. Theoretical investigations of $Pt_1@CeO_2$ single-atom catalyst for CO oxidation. *J. Phys. Chem. C* **121**, 11281–11289 (2017).
30. Zuo, J.-M., Kim, M., O'Keeffe, M. & Spence, J. Direct observation of *d*-orbital holes and Cu–Cu bonding in Cu_2O. *Nature* **401**, 49–52 (1999).
31. Zhang, W. et al. Emerging dual-atomic-site catalysts for efficient energy catalysis. *Adv. Mater.* **33**, 2102576 (2021).
32. Campos, J. Bimetallic cooperation across the periodic table. *Nat. Rev. Chem.* **4**, 696–702 (2020).
33. Klapars, A., Antilla, J. C., Huang, X. & Buchwald, S. L. A general and efficient copper catalyst for the amidation of aryl halides and the *N*-arylation of nitrogen heterocycles. *J. Am. Chem. Soc.* **123**, 7727–7729 (2001).
34. Satyanarayana, K., Srinivas, K., Himabindu, V. & Reddy, G. M. A scaleable synthesis of dutasteride: a selective 5α-reductase inhibitor. *Org. Process Res. Dev.* **11**, 842–845 (2007).
35. Kim, D., Jun, H., Lee, H., Hong, S.-S. & Hong, S. Development of new fluorescent xanthines as kinase inhibitors. *Org. Lett.* **12**, 1212–1215 (2010).
36. Zheng, J., Cui, W.-J., Zheng, C. & You, S.-L. Synthesis and application of chiral spiro Cp ligands in rhodium-catalyzed asymmetric oxidative coupling of biaryl compounds with alkenes. *J. Am. Chem. Soc.* **138**, 5242–5245 (2016).
37. Cheng, J. K., Xiang, S.-H., Li, S., Ye, L. & Tan, B. Recent advances in catalytic asymmetric construction of atropisomers. *Chem. Rev.* **121**, 4805–4902 (2021).
38. Bhunia, S., Pawar, G. G., Kumar, S. V., Jiang, Y. & Ma, D. Selected copper-based reactions for C–N, C–O, C–S, and C–C bond formation. *Angew. Chem. Int. Ed.* **56**, 16136–16179 (2017).
39. Gutmann, B., Cantillo, D. & Kappe, C. O. Continuous-flow technology—a tool for the safe manufacturing of active pharmaceutical ingredients. *Angew. Chem. Int. Ed.* **54**, 6688–6728 (2015).

Methods

Synthesis of PCN

Bulk PCN was prepared by calcining dicyandiamide at 550 °C (2.3 °C min^{-1} heating rate) in a crucible for 3 h in static air. Exfoliated PCN was obtained by thermal exfoliation at 500 °C (5 °C min^{-1} heating rate) for 5 h in static air. The exfoliation procedure was repeated several times until the PCN was exfoliated efficiently.

Synthesis of Cu_g/PCN

$CuCl_2$ (0.64 g) and exfoliated PCN (0.70 g) were dispersed in 200 ml formamide, sonicated for 10 min and then stirred in an oil bath (120 °C) for 12 h, following centrifugation and washing thoroughly by ethanol several times. The oven-dried powder (80 °C) was subsequently heated to 500 °C with a heating rate of 2 °C min^{-1} and kept for 5 h with the protection of N_2 flow. Cu_i/PCN with Cu contents of 0.2, 0.9, 1.8, 8.0 and 10.8 wt% were prepared using 0.2, 1.0, 2.0, 10.0 and 15.0 wt% Cu feeding, respectively.

Material characterization

Wide-angle XRD patterns were collected on a Bruker D8 Focus Powder X-ray diffractometer using Cu Kα radiation (40 kV, 40 mA) at room temperature. ADF-STEM imaging was carried out in an aberration-corrected JEOL ARM-200F system equipped with a cold field emission gun operating at 60 kV. XPS measurements were carried out in a custom-designed ultrahigh-vacuum system with a base pressure lower than 2×10^{-10} mbar. Al Kα ($h\nu$ = 1,486.7 eV) was used as the excitation source for XPS. The atomic force microscopy image was acquired on a Bruker FastScan AFM using TappingMode. The metal content in all the catalysts was measured by an inductively coupled plasma atomic emission spectrometer. FTIR spectra were performed at 25 °C on a Bruker Equinox 55 spectrometer equipped with a mercury cadmium telluride detector. X-band EPR spectra were obtained with a JEOL (FA200) spectrometer. ^{1}H, ^{13}C and ^{19}F nuclear magnetic resonance spectra were recorded on Bruker Avance Neo 400 or 500 spectrometers. The STM experiments were conducted in ultrahigh-vacuum conditions (base pressure $<2 \times 10^{-9}$ mbar) at 4.4 K using a Scienta Omicron LT STM system. The XANES and EXAFS measurements were carried out at the XAFCA beamline of the Singapore Synchrotron Light Source (SSLS)[40]. A Si(111) double-crystal monochromator was used to filter the X-ray beam. High-resolution XANES was performed using the third harmonic of the Si(111) double-crystal monochromator. Copper foil was used for the energy calibration and all samples were measured under transmission mode. EXAFS oscillations $\chi(k)$ were extracted and analysed using the Demeter software package[41].

For cross-coupling reactions, all the reactants and catalysts were added in a nitrogen-filled glovebox to avoid potential performance losses owing to substrate instability in the presence of oxygen or, in particular, trace amounts of water.

C–N bond formation

An oven-dried screw-top reaction tube was equipped with a stir bar. Aryl halide (0.2 mmol), nitrogen-based nucleophile (0.24 mmol for N-heterocyclic compounds, 0.3 mmol for primary and secondary amines), Cu_g/PCN (1.0 mg, 1.4 mol% Cu), 0.4 mmol base (K_3PO_4 for N-heterocyclic compounds, NaOH for primary and secondary amines) and anhydrous dimethyl sulfoxide (DMSO; 1.0 ml) were sequentially added. The reaction tube was sealed with a Teflon-lined screw cap, removed from the glovebox, placed in an oil bath preheated to 110 °C and stirred for 28 h. After cooling to room temperature, the reaction cap was removed and the reaction mixture was concentrated in vacuo with the aid of a rotary evaporator. The resulting residue was then purified by silica gel column chromatography to give the pure product.

C–O bond formation

An oven-dried screw-top reaction tube was equipped with a stir bar. Aryl iodide (0.2 mmol), alcohol (0.4 mmol, for di-halide aromatic ring, 0.8 mmol), Cu_g/PCN (1.0 mg, 1.4 mol% Cu), KO*t*Bu (0.3 mmol, for di-halide aromatic ring, 0.6 mmol) and anhydrous dioxane (2.0 ml) were sequentially added. The reaction tube was sealed with a Teflon-lined screw cap, removed from the glovebox, placed in an oil bath preheated to 80 °C and stirred for 18 h. After cooling to room temperature, the reaction cap was removed and the reaction mixture was concentrated in vacuo with the aid of a rotary evaporator. The resulting residue was then purified by silica gel column chromatography to give the pure product.

C–C bond formation

An oven-dried screw-top reaction tube was equipped with a stir bar. Aryl halide (0.2 mmol), alkyne (0.3 mmol, for di-halide aromatic ring, 0.6 mmol), Cu_g/PCN (1.0 mg, 1.4 mol% Cu), $Cs(OH)_2.H_2O$ (0.3 mmol, for di-halide aromatic ring, 0.6 mmol) and anhydrous DMSO (1.0 ml) were sequentially added. The reaction tube was sealed with a Teflon-lined screw cap, removed from the glovebox, placed in an oil bath preheated to 110 °C and stirred for 28 h. After cooling to room temperature, the reaction cap was removed and the reaction mixture was concentrated in vacuo with the aid of a rotary evaporator. The resulting residue was then purified by silica gel column chromatography to give the pure product.

C–S bond formation

An oven-dried screw-top reaction tube was equipped with a stir bar. Aryl halide (0.2 mmol), mercaptan/thiophenol (0.3 mmol), Cu_g/PCN (1.0 mg, 1.4 mol% Cu), NaO*t*Bu (0.30 mmol) and anhydrous dioxane (2.0 ml) were sequentially added. The reaction tube was sealed with a Teflon-lined screw cap, removed from the glovebox, placed in an oil bath preheated to 80 °C and stirred for 18 h. After cooling to room temperature, the reaction cap was removed and the reaction mixture was concentrated in vacuo with the aid of a rotary evaporator. The resulting residue was then purified by silica gel column chromatography to give the pure product.

Azide–alkyne cycloaddition

Azide–alkyne cycloaddition was carried out in a 10-ml glass tube with Cu_g/PCN catalyst (1 mg, 1.4 mol% Cu), 0.2 mmol of aryl acetylene, 0.6 mmol (1.2 mmol for di-aryl acetylene) of benzyl azide, decane (0.2 mmol) and 3 ml of a 1:1 water/acetonitrile mixture and stirred at 60 °C for 24 h. After cooling to room temperature, the mixture was diluted with water and extracted with dichloromethane. The crude product was analysed by gas chromatography–mass spectrometry for determination of the yield.

Recycling test

4-Iodotoluene (20.0 mmol, 4,360 mg), ethanol (40.0 mmol, 1,840 mg), Cu_g/PCN (100 mg, 1.4 mol% Cu), KO*t*Bu (30 mmol, 3,368 mg), decane (10.0 mmol, 1,950 µl) and anhydrous dioxane (200 ml) were sequentially added to an oven-dried screw-top reaction bottle equipped with a stir bar. The reaction bottle was sealed with a Teflon-lined screw cap, removed from the glovebox, placed in an oil bath preheated to 80 °C and stirred for 8 h. After cooling to room temperature, the bottle was allowed to stand for 1 h. The reaction cap was then removed, an aliquot of the solution transferred into a vial, diluted with EtOAc and analysed by gas chromatography to determine the yield. The remaining reaction mixture was removed by vacuum filtration using nylon filter membranes. Before use in the next cycle reaction, the catalyst was washed in dioxane, EtOH and deionized water three times and dried overnight at 80 °C.

Continuous-flow synthesis

The continuous-flow reactions were conducted in a tubular reactor. 250 mg of Cu_g/PCN (40–100 mesh particles) and 250 mg quartz sand/celite at each end was packed in a steel/quartz column reactor and the mixture of reactants, bases and solvents was pumped through

the column at a certain flow rate. The real-time yield of product was detected by gas chromatography–mass spectrometry.

In situ X-ray absorption spectroscopy

In a nitrogen-filled glovebox, an oven-dried screw-top reaction tube was equipped with a stir bar. 4-iodobenzene (1.0 mmol), ethanol (2.0 mmol), Cu_g/PCN (5.0 mg), KO*t*Bu (1.5 mmol) and anhydrous dioxane (5.0 ml) were sequentially added. The reaction tube was sealed with a Teflon-lined screw cap, removed from the glovebox, placed in an oil bath preheated to 80 °C and stirred for 3 h. After that, the mixture was quickly transferred to a plastic bag for XAFS measurement.

In situ EPR spectroscopy

In a nitrogen-filled glovebox, an oven-dried quartz EPR tube was equipped with a stir bar. 4-iodobenzene (0.05 mmol), ethanol (0.1 mmol), Cu_g/PCN (4.0 mg), KO*t*Bu (0.075 mmol) and anhydrous dioxane (0.5 ml) were sequentially added. The reaction tube was sealed with a screw cap, removed from the glovebox and placed in an oil bath preheated to 80 °C under stirring. For each indicated time, the EPR tube was transferred from the oil bath to the EPR spectrometer and the corresponding measurement taken. After collecting the data, the EPR tube was retransferred to the oil bath for continuing reactions.

Computational details

The quantum-chemical studies were carried out at the level of Kohn–Sham DFT using two types of theoretical formalism, the periodic DFT approach and the molecular DFT approach for a selected cluster model. These two approaches provide more comprehensive computational data for understanding the geometric structures, electronic structures, chemical bonding and catalytic mechanism. The periodic DFT calculations were performed with the Vienna Ab initio Simulation Package (VASP)[42]. These first-principles calculations under spin-polarized Kohn–Sham formulism were carried out for the structure optimizations, electronic-structure analysis and transition-state search with climbing image nudged elastic band[43]. The generalized gradient approximation in Perdew–Burke–Ernzerhof exchange-correlation functional[44], the projector-augmented wave method[45] and a plane-wave basis set with a cutoff energy of 450 eV were used in all the calculations. The convergence criterion for structural relaxations and climbing image nudged elastic band was set to 0.01 eV $Å^{-1}$ and 0.05 eV $Å^{-1}$, respectively. A vacuum layer of 15 Å in the direction perpendicular to PCN film was included to avoid artificial interaction between the neighbouring images. $5 \times 5 \times 1$ *k*-point sampling was applied in all calculations. A 2×2 supercell of PCN structure was adopted to model the Cu-doped PCN 2D film. The supercell used in the calculation is shown in Supplementary Fig. 7. The adsorption energy is defined as $E_{ads} = E(\text{adsorbed}) - E(\text{separated})$, which means stronger adsorption with more negative adsorption energy. The calculated charge density distributions and PDOS of the single-atom Cu and two-atom Cu (geminal) doped carbon–nitrogen 2D material are shown in Extended Data Fig. 7.

The molecular DFT calculations were carried out on the cluster model constructed to compare with the periodic DFT calculations, as shown in Supplementary Fig. 7b. Spin-restricted and spin-unrestricted (polarized) Kohn–Sham calculations were respectively carried out for closed-shell singlet states and open-shell singlet/triplet states using the Gaussian 16 suite of programs[46]. The polarized split-valence 6-31G(d) Gaussian basis sets were used for the C, N, O and H atoms[47]. The effective core potential of LANL2DZ[48] was adopted for Cu, together with the LANL2DZ basis set for the valence electrons of Cu [Ne]$3s^2 3p^6 3d^6 4s^2$. Harmonic vibrational frequencies were obtained at the same levels in this work to check the properties of the stationary points. All of the structures discussed in this work are minimal or transition states on the corresponding potential energy surfaces, as confirmed by zero or one imaginary frequency, respectively. To further refine the electronic energies, the single-point calculations on the optimized geometries were also performed using the hybrid B3LYP functional when specified[49,50]. We also plotted the radial distribution probability density (Supplementary Fig. 9), $D(r) = r^2R(r)^2$, of Cu(II) atomic orbitals to explain the chemical bonding interaction of geminal Cu…Cu when the distance is changed.

The adsorption energy (E_{ads}) for molecule M on the GACs was defined as

$$E_{ads} = E_{M\text{-}GAC} - E_{GAC} - E_M$$

in which $E_{M\text{-}GAC}$, E_{GAC} and E_M are the total energy for GACs with the M-molecule adsorbed, the GACs and the absorption molecule, respectively.

To explore the catalytic reaction mechanism of various chemical reactions on GACs, we have chosen to focus on C–O coupling reactions. The reaction between C_6H_5I and CH_3OH was selected as an example and the energy profiles calculated with Perdew–Burke–Ernzerhof functional for the various pathways and processes are shown in Supplementary Figs. 8–12. Both the direct dehalogenation and dehydrogenation of C_6H_5I and CH_3OH and the indirect ones with the help of strong base of KO*t*Bu were studied. Two reaction pathways (indirect and direct pathways) for C–O coupling between $*C_6H_5$ and CH_3O* were also explored. Through the indirect pathway, C–O coupling of CH_3O* and $*C_6H_5$ to form $C_6H_5OCH_3$ is much more difficult than in the direct pathway, in which C–O coupling is facilitated by dynamic formation of a direct Cu–Cu 4*s*–4*s* bond. The latter represents a new reaction mechanism for C–O coupling by means of the disproportional process of copper oxidation state from Cu(II)–Cu(II) to Cu(III)–Cu(I). The atomic numbering of the Cu_A…Cu_B active sites together with the N-atoms of GACs, as well as the calculated bond distances and Wiberg bond orders for intermediate states IS5 and IS6, are listed in Supplementary Table 5. The Mulliken spin-density populations of the atoms in the open-shell intermediates ^{3}IS3 and ^{3}IS4 are listed in Supplementary Table 7 to facilitate the assignment of the oxidation states of Cu_A…Cu_B active sites in the disproportional process. Here the superscripts 1 and 3 (for example, in ^{3}IS3 and ^{3}IS4) indicate the spin multiplicity 2S + 1 of the system.

LCA

LCA followed the four LCA phases in the ISO 14040/14044 standards[51,52]. The goal (step 1) was to estimate the environmental impacts of two alternative catalytic pathways (that is, heterogeneously and homogeneously catalysed) for the synthesis of product **1** (1-(naphthalen-1-yl)-1*H*-imidazole) through an Ullmann-type C–N coupling reaction. Both pathways use the same substrates (1-iodonaphthalene and 1*H*-imidazole) but implement different reaction conditions, including solvents (dimethyl sulfoxide or N-methyl-2-pyrrolidone, respectively), to synthesize 1 kg of product **1** (the functional unit). The heterogeneous reaction uses the Cu_g/PCN GAC developed in this work, for which the homogeneous catalytic system consisted of Cu_2O with 4,7-dimethoxy-1,10-phenanthroline as the ligand ($Cu_2O + L_1$; Supplementary Table 2). A cradle-to-gate scope was adopted, that is, the LCA covers all the emissions associated with the upstream activities in the synthesis of substrates, solvents and catalysts for both systems until the generation of product **1**, while omitting its posterior use and disposal stages (which would be the same in both cases). No recycling was assumed for the reaction mixture in either of the routes in the baseline scenarios. However, the effect of reusing the catalyst and solvent (that is, reducing the required amounts of these components) was explored in a sensitivity analysis considering up to 100 cycles (Supplementary Fig. 23).

In the life-cycle inventory (step two), we used experimental values complemented with mass balances based on stoichiometric coefficients of upstream synthesis steps to estimate the whole range of inputs in the foreground system. In essence, mass balances were applied recursively in the synthesis tree of the two catalysts and one

of the reactants (that is, 1-iodonaphthalene) until reaching compounds available in ecoinvent v3.9 (ref. 53), from where background data of the surrounding activities providing inputs to the foreground system were retrieved using the cutoff modelling choice (more details are available at https://ecoinvent.org/the-ecoinvent-database). In the life cycle impact assessment phase (step three), we computed the 100-year global warming potential (GWP100), measured in kg of CO_2 equivalents (kg_{CO2eq}), considering short-lived climate forcers. To this end, we followed the Intergovernmental Panel on Climate Change of the United Nations[54], which estimates the potential of climate change induced by greenhouse gas emissions. Moreover, we complement the impact analysis with the end points of the ReCiPe2016 (ref. 55), assessing the damage on three main areas of protection; human health, ecosystems quality and resource availability. Finally, in the fourth LCA phase, the results were interpreted, identifying hotspots and providing conclusions and recommendations. All of the LCA calculations were implemented in Brightway2 v2.4.1 (ref. 56).

Data availability

All data are available in the manuscript or in the Supplementary information. The data for the LCA analysis are deposited in the Zenodo repository: https://doi.org/10.5281/zenodo.8277667.

40. Du, Y. et al. XAFCA: a new XAFS beamline for catalysis research. *J. Synchrotron Radiat.* **22**, 839–843 (2015).
41. Ravel, B. & Newville, M. ATHENA, ARTEMIS, HEPHAESTUS: data analysis for X-ray absorption spectroscopy using IFEFFIT. *J. Synchrotron Radiat.* **12**, 537–541 (2005).
42. Kresse, G. & Furthmüller, J. Efficient iterative schemes for *ab initio* total-energy calculations using a plane-wave basis set. *Phys. Rev. B* **54**, 11169 (1996).
43. Henkelman, G., Uberuaga, B. P. & Jónsson, H. A climbing image nudged elastic band method for finding saddle points and minimum energy paths. *J. Chem. Phys.* **113**, 9901–9904 (2000).
44. Perdew, J. P., Burke, K. & Ernzerhof, M. Generalized gradient approximation made simple. *Phys. Rev. Lett.* **77**, 3865 (1996).
45. Kresse, G. & Joubert, D. From ultrasoft pseudopotentials to the projector augmented-wave method. *Phys. Rev. B* **59**, 1758 (1999).
46. Frisch, M. J. et al. *Gaussian 16* (Gaussian, Inc., 2016).
47. Francl, M. M. et al. Self-consistent molecular orbital methods. XXIII. A polarization-type basis set for second-row elements. *J. Chem. Phys.* **77**, 3654–3665 (1982).
48. Hay, P. J. & Wadt, W. R. Ab initio effective core potentials for molecular calculations. Potentials for K to Au including the outermost core orbitals. *J. Chem. Phys.* **82**, 299–310 (1985).
49. Becke, A. D. Density-functional exchange-energy approximation with correct asymptotic behavior. *Phys. Rev. A* **38**, 3098 (1988).
50. Lee, C., Yang, W. & Parr, R. G. Development of the Colle-Salvetti correlation-energy formula into a functional of the electron density. *Phys. Rev. B* **37**, 785 (1988).
51. ISO 14040:2006. Environmental management — life cycle assessment — principles and framework. International Organization for Standardization (ISO) (2006).
52. ISO 14044:2006. Environmental management — life cycle assessment — requirements and guidelines. International Organization for Standardization (ISO) (2006).
53. Wernet, G. et al. The ecoinvent database version 3 (part I): overview and methodology. *Int. J. Life Cycle Assess.* **21**, 1218–1230 (2016).
54. Forster, P. et al. in *Climate Change 2021: The Physical Science Basis. Contribution of Working Group I to the Sixth Assessment Report of the Intergovernmental Panel on Climate Change* (eds Masson-Delmotte, V. et al.) Ch. 7, 923–1054 (Cambridge Univ. Press, 2021).
55. Huijbregts, M. A. et al. ReCiPe2016: a harmonised life cycle impact assessment method at midpoint and endpoint level. *Int. J. Life Cycle Assess.* **22**, 138–147 (2017).
56. Mutel, C. Brightway: an open source framework for life cycle assessment. *J. Open Source Softw.* **2**, 236 (2017).

Acknowledgements J. Lu acknowledges support from MOE Tier 2 (MOE-T2EP50121-0008) and the Agency for Science, Technology and Research (A*STAR) under its MTC IRG grant (project nos. M22K2c0082 and A20E5c0096). Y. Zhu acknowledges support from Pharma Innovation Programme Singapore (PIPS, A*STAR-IAF-PP A19B3a0016 and A20B3a0107). M.J.K. acknowledges support from MOE Tier 2 (MOE-T2EP10122-0003). R.Z. acknowledges financial support from the National Natural Science Foundation of China (grant 51825201). S.M., V.T., G.G.-G. and J.P.-R. acknowledge funding from NCCR Catalysis (grant 180544), a National Centre of Competence in Research funded by the Swiss National Science Foundation. Jun Li acknowledges financial support from the National Natural Science Foundation of China (grant 22033005), NSFC Center for Single-Atom Catalysis, National Key R&D Project (nos. 2022YFA1503900 and 2022YFA1503000) and the Guangdong Provincial Key Laboratory of Catalysis (no. 2020B121201002). Q.Y. acknowledges financial support by the Natural Science Basic Research Program of Shaanxi (2021JCW-20 and 2022KJXX-18). We acknowledge the computational resources supported by the Center for Computational Science and Engineering (SUSTech), Tsinghua National Laboratory for Information Science and Technology and the National Supercomputing Centre (NSCC) Singapore. Q.Y. is grateful for the hospitality of Tsinghua University during her sabbatical visit.

Author contributions J. Lu supervised the project and organized the collaboration. X.H. and J. Lu conceived the research and proposed geminal-atom catalysis. X.H. designed the experiments and synthesized the materials. Jun Li and Q.Y. conceived the Cu–Cu bonding reaction mechanism and carried out quantum-chemical calculations. N.G. and C.Z. carried out theoretical calculations of the periodic structures. Y. Zhe., X.H. and Y. Zhu discovered the catalytic activity. M.J.K. and X. Luo conducted the comparison studies and synthetic applications. S.X. performed the XAFS measurement and structural analysis. X.Z. and Y.C. performed the electron microscopy experiments and data analysis. X.S. and X.P. performed the scanning tunnelling microscope experiments. J.W., X. Lo and M.W. performed the continuous-flow synthesis. V.T., J.P.-R. and G.G.-G. performed the LCA analysis and interpreted the results. S.M. and J.P.-R. advised on the experiments, methodologies and data presentation. L.R., Jing Li, P.H., H.L., J.S. and R.Z. assisted with materials characterization and data analysis. X.H. wrote the draft, with the assistance of Q.Y., Y. Zhe. and S.M. All authors discussed the results and edited and commented on the manuscript.

Competing interests The authors declare no competing interests.

Additional information

Supplementary information The online version contains supplementary material available at https://doi.org/10.1038/s41586-023-06529-z.

Correspondence and requests for materials should be addressed to Shibo Xi, Javier Pérez-Ramírez, Ming Joo Koh, Ye Zhu, Jun Li or Jiong Lu.

Peer review information *Nature* thanks Jagadeesh Rajenahally and the other, anonymous, reviewer(s) for their contribution to the peer review of this work.

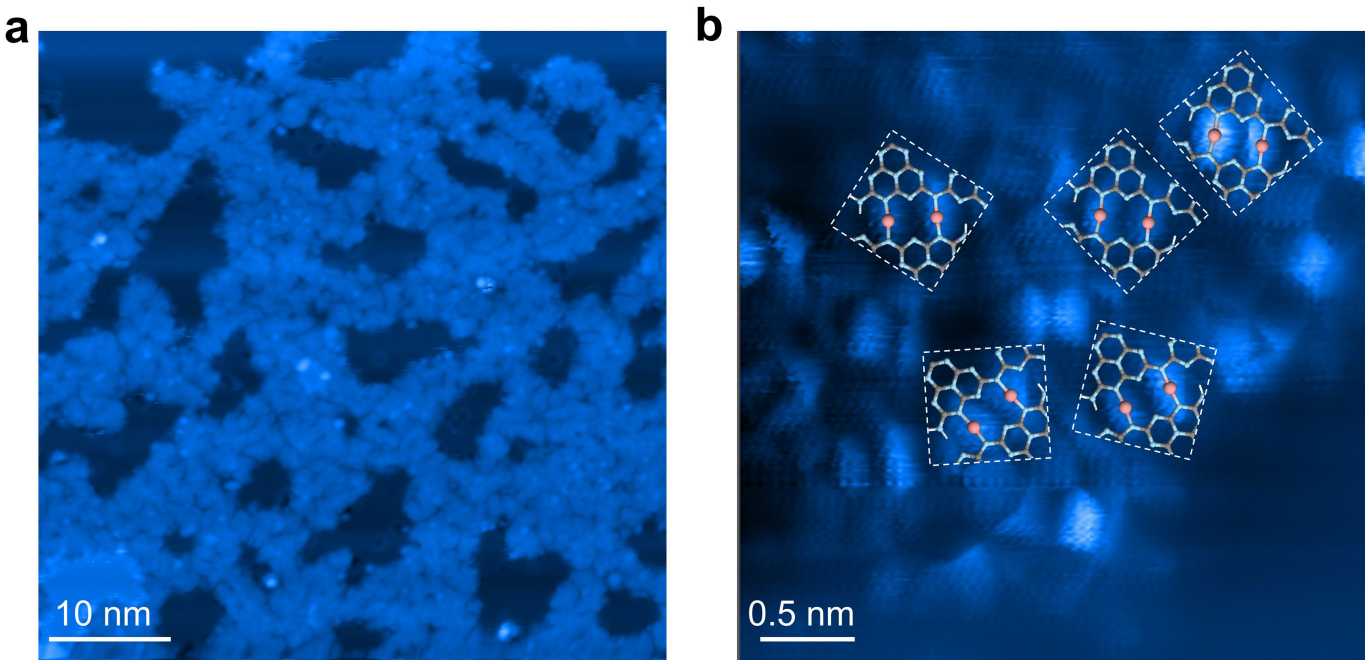

Extended Data Fig. 1 | STM characterization of Cu_g/PCN. a, Overview STM image after annealing PCN on Cu(111) at 370 K, $V = 2.0$ V, $I = 20$ pA. **b**, Corresponding constant-height STM image with a CO-functionalized tip ($V = 5$ mV, $\Delta z = -20$ pm; set point before turning off feedback, $V = 5$ mV, $I = 200$ pA).

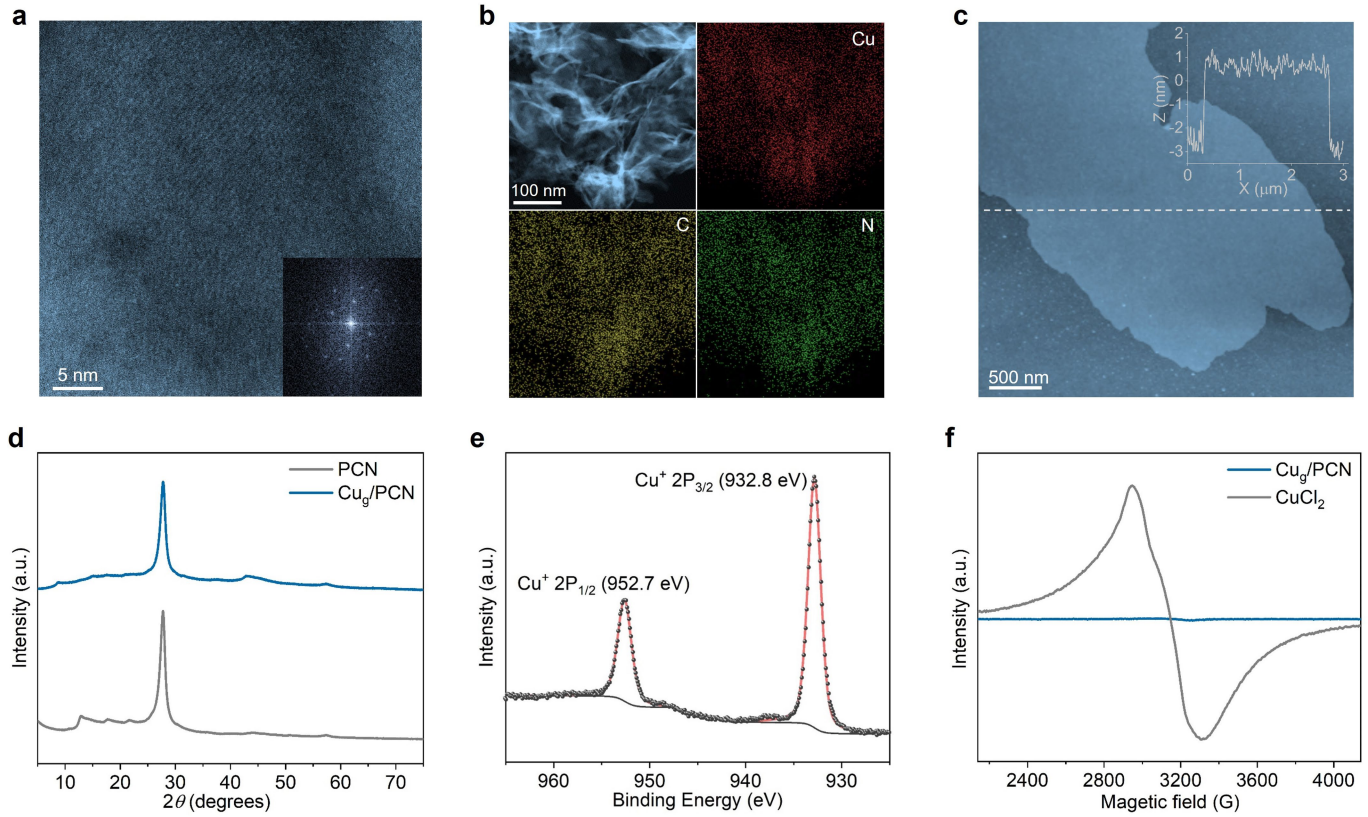

Extended Data Fig. 2 | Characterization of Cu$_g$/PCN. a, High-resolution TEM image with the corresponding Fourier transform diffraction pattern inset. **b**, ADF-STEM image and corresponding elemental maps. **c**, Atomic force microscopy image of Cu$_g$/PCN with height profile inset. **d**, XRD patterns of PCN and Cu$_g$/PCN. **e**, Cu 2*p* XPS spectra of Cu$_g$/PCN. The peaks at 932.8 eV and 952.7 eV are assigned to Cu(I). The solid red line and dotted black line represent the experiment and fitting curves, respectively. **f**, EPR spectra of Cu$_g$/PCN and the reference $CuCl_2$.

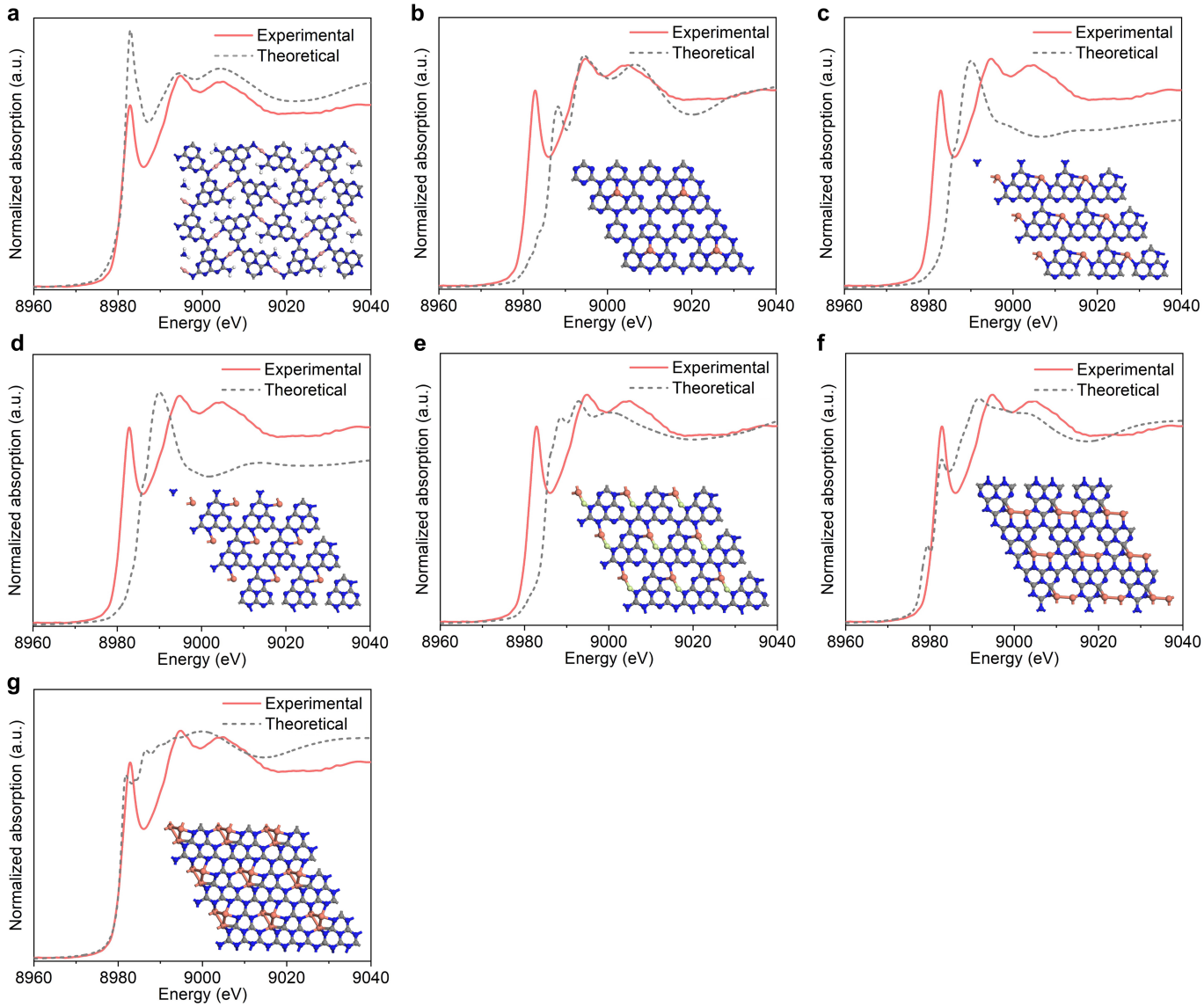

Extended Data Fig. 3 | Comparison of the experimental and modelled Cu K-edge XANES spectra. The corresponding DFT-modelled atomic structures are shown in the insets. Colour code: C, grey; N, blue; O, green; Cu, orange; H, white.

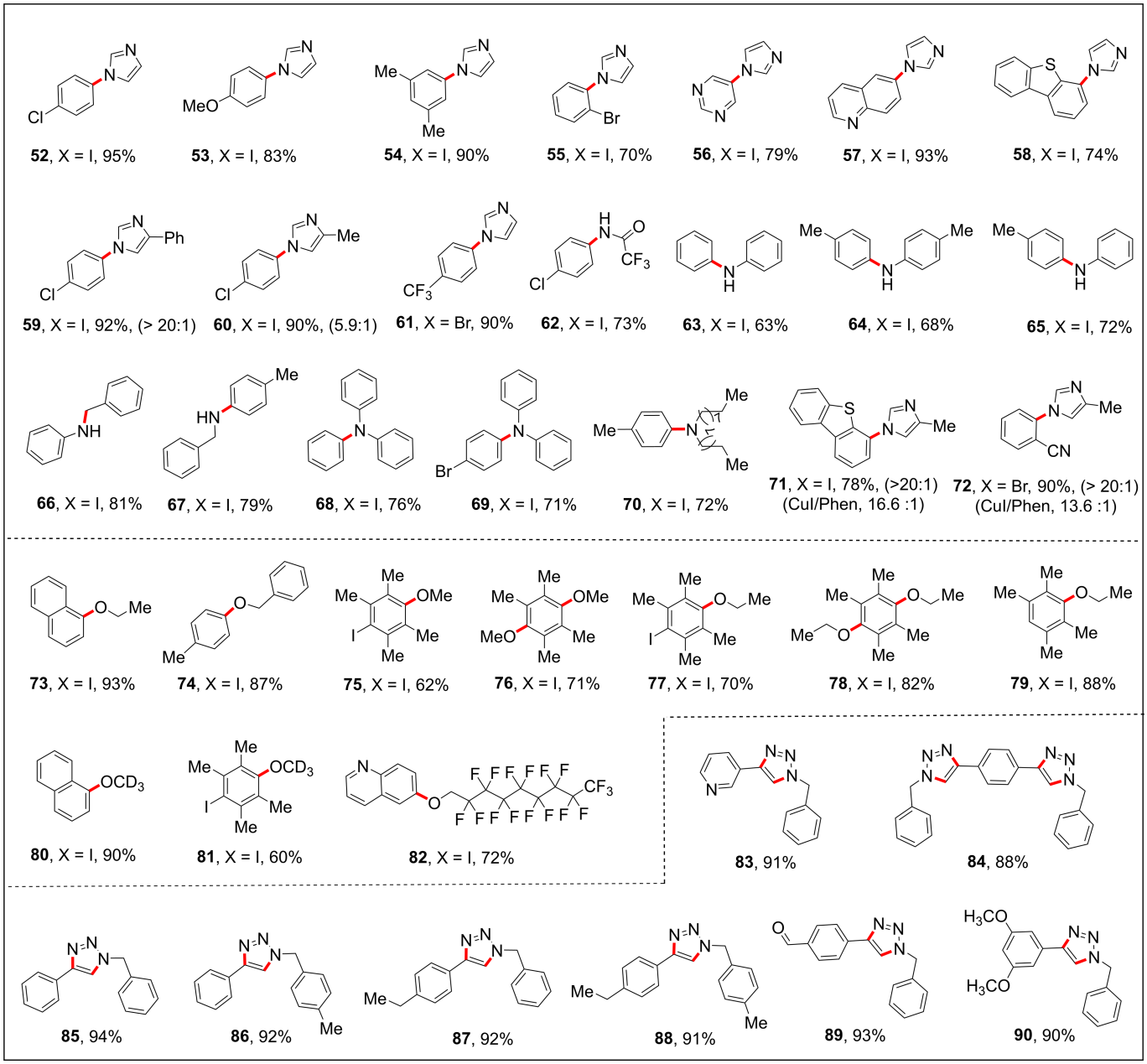

Extended Data Fig. 4 | Substrate scope of Cu_g/PCN-catalysed cross-coupling and cycloaddition. Product isolated yields obtained in Cu_g/PCN-catalysed C–N (**52**–**72**) and C–O bond formations (**73**–**82**). Products yields for Cu_g/PCN-catalysed azide–alkyne cycloadditions (**83**–**90**) determined by gas chromatography.

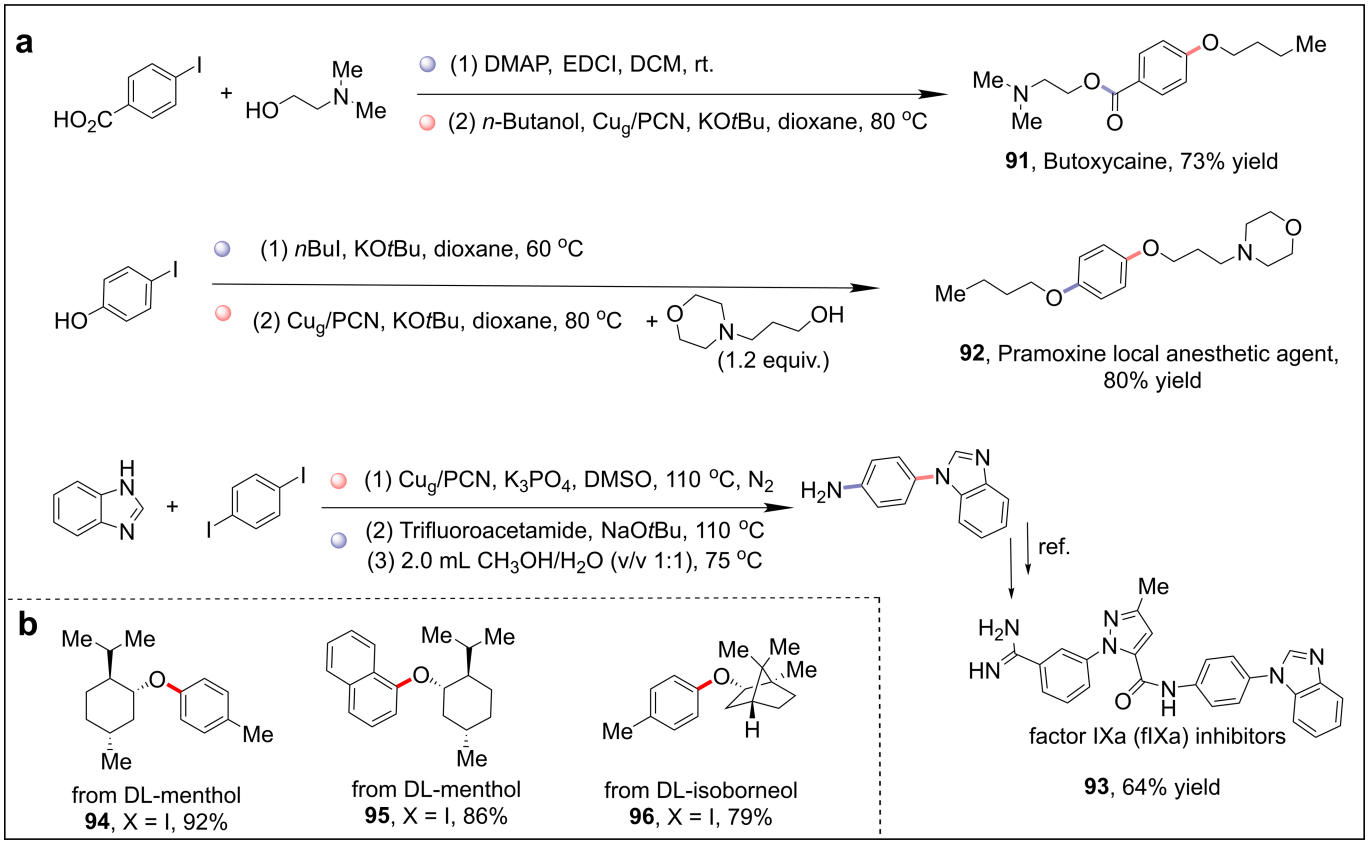

Extended Data Fig. 5 | Cu$_g$/PCN-catalysed pharmaceutical and biorelevant molecules. a, Synthesis of pharmaceutical compounds (**91**–**93**) in multisteps and one-pot manner. **b**, Synthesis of biorelevant molecules (**94**–**96**) from natural products.

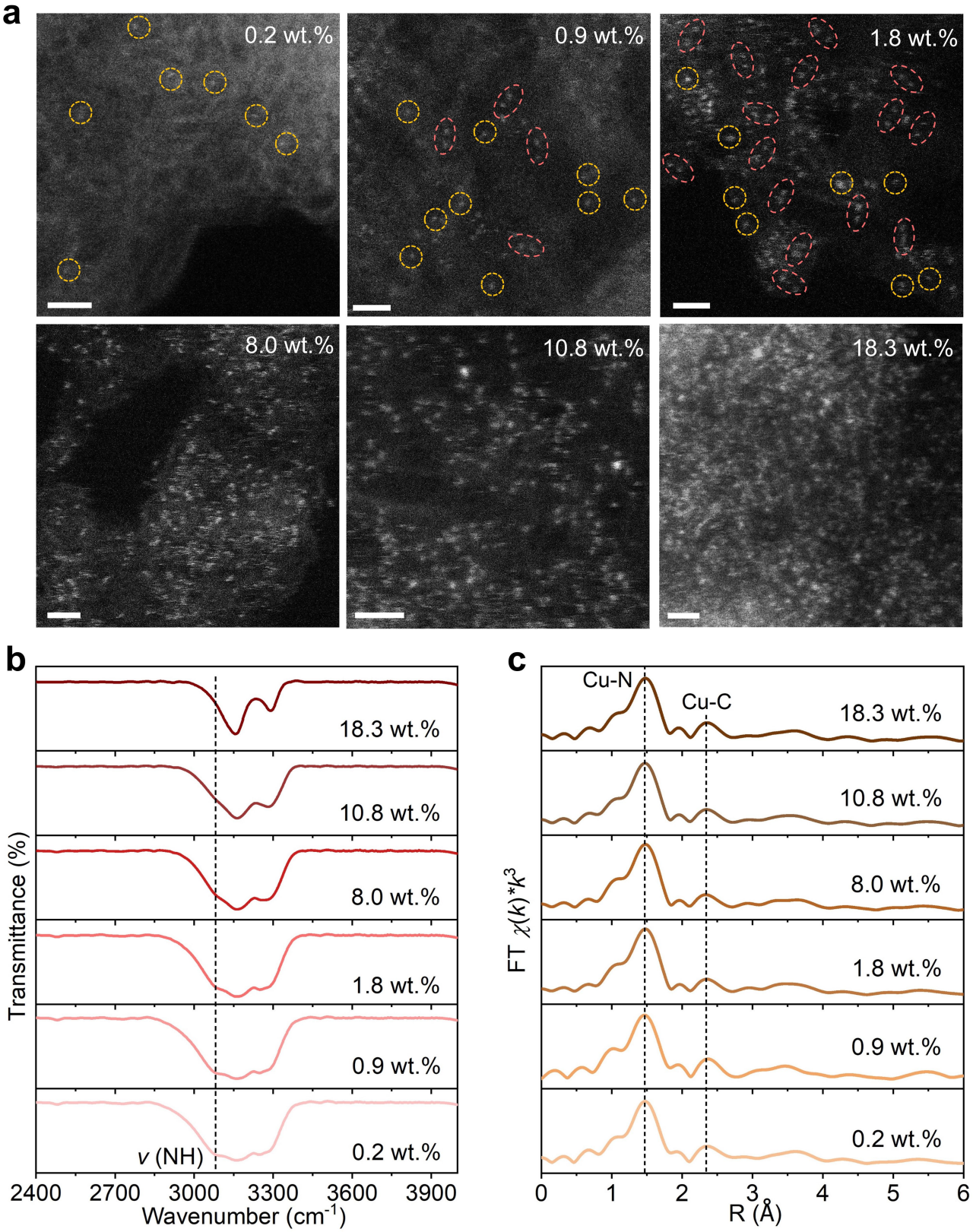

Extended Data Fig. 6 | Characterization of Cu_1/PCN with different Cu contents. ADF-STEM images (scale bar, 1 nm) (**a**), FTIR spectra (**b**) and Fourier-transformed EXAFS spectra (**c**) of Cu_1/PCN samples with different Cu contents. Red and yellow dashed lines encircle GAC and SAC sites, respectively.

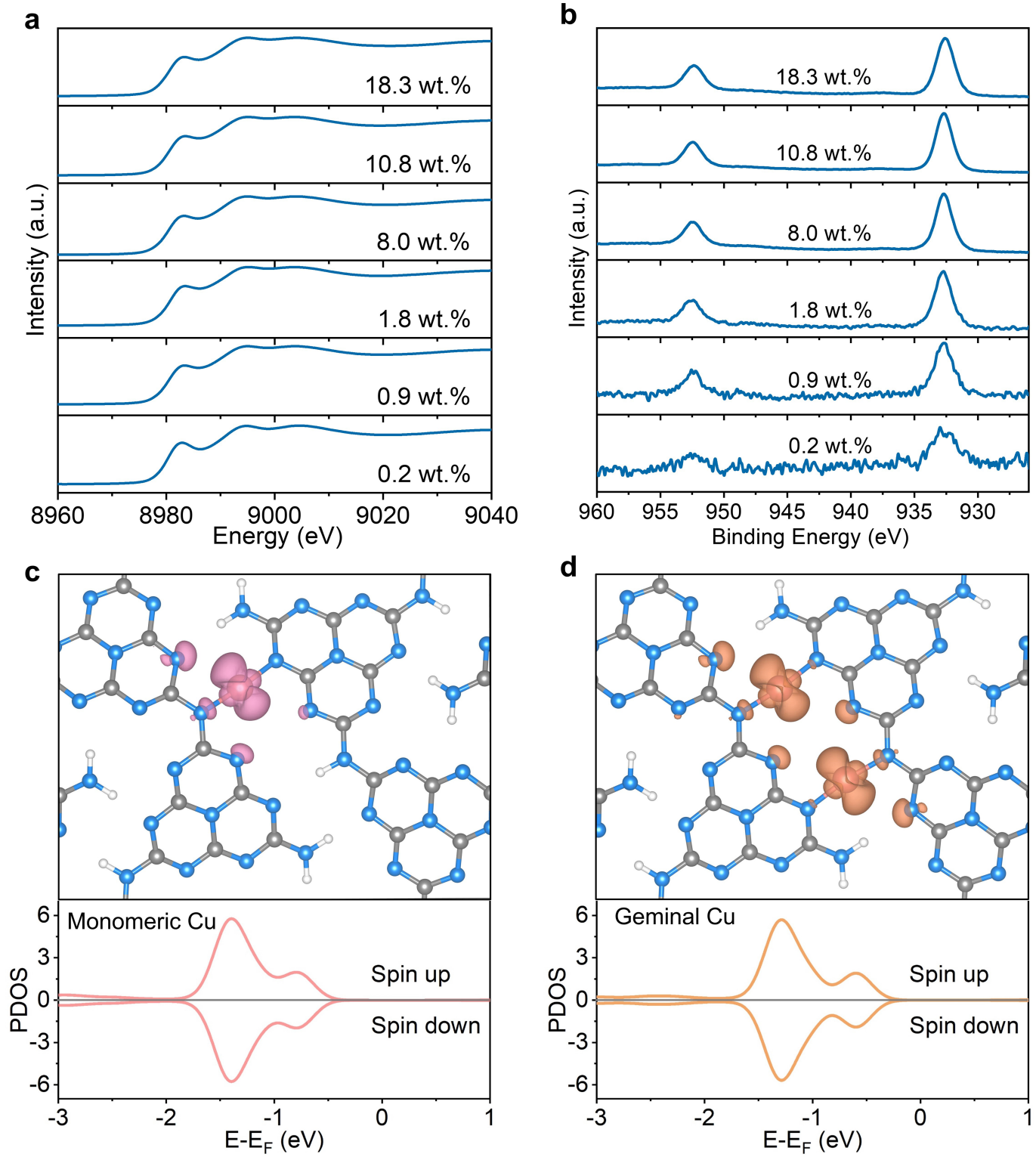

Extended Data Fig. 7 | Electronic structure of Cu_1/PCN with different Cu contents. Cu K-edge XANES (**a**) and Cu 2*p* XPS (**b**) spectra of Cu_1/PCN samples with different Cu contents. **c**,**d**, Charge density distributions and PDOS of monomeric (**c**) and geminal (**d**) Cu sites, respectively. Colour code: Cu, pink; C, grey; N, blue; H, white.

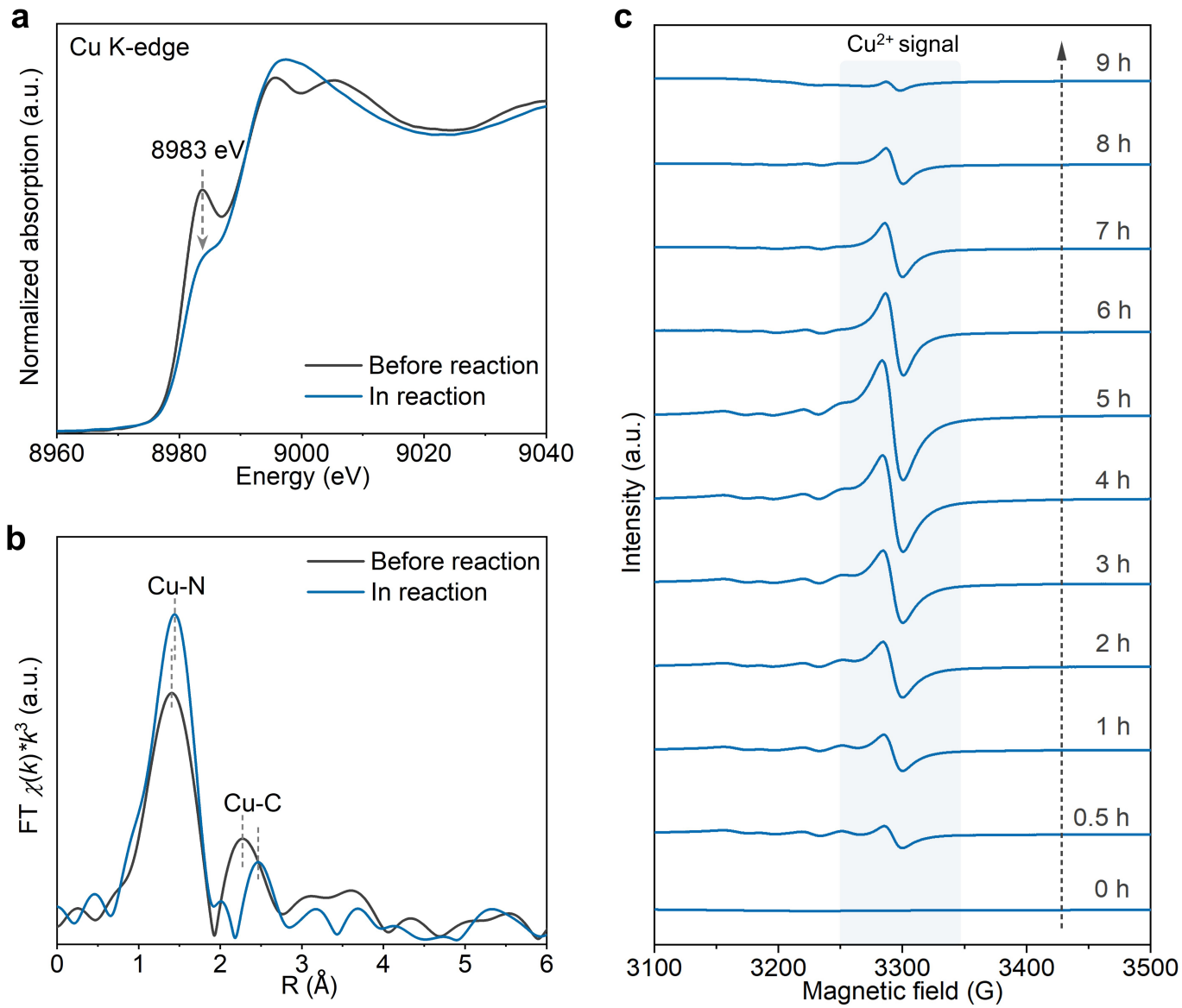

Extended Data Fig. 8 | In situ XANES and EPR spectra during C–O coupling reaction. a,**b**, In situ Cu K-edge XANES (**a**) and Fourier-transformed EXAFS (**b**) spectra of Cu_g/PCN catalyst measured before and in the C–O coupling reaction, respectively. **c**, In situ EPR spectra of Cu_g/PCN recorded at different times in the C–O coupling reaction. The chemical state change of Cu_g/PCN during the C–O cross-coupling reaction cycle was clearly seen from Cu K-edge XANES. A distinct weakening of the feature peak at 8,983 eV and an increase of the main peak at 8,996 eV indicate that the valence state of Cu increases during the reaction, which is related to the successful adsorption of 4-iodotoluene or methanol. Correspondingly, the intensity of the main peak related to the first coordination sphere in the Fourier-transformed EXAFS spectra increases, evidencing the increased coordination number of Cu. The change in the chemical valence state of Cu during the reaction cycle is further explained by in situ EPR spectroscopy. EPR-silent Cu(I) is first oxidized to EPR-sensitive Cu(II) with a gradually enhanced signal intensity and then reduced to the original Cu(I) state during a complete reaction process, in line with the in situ XAFS results.

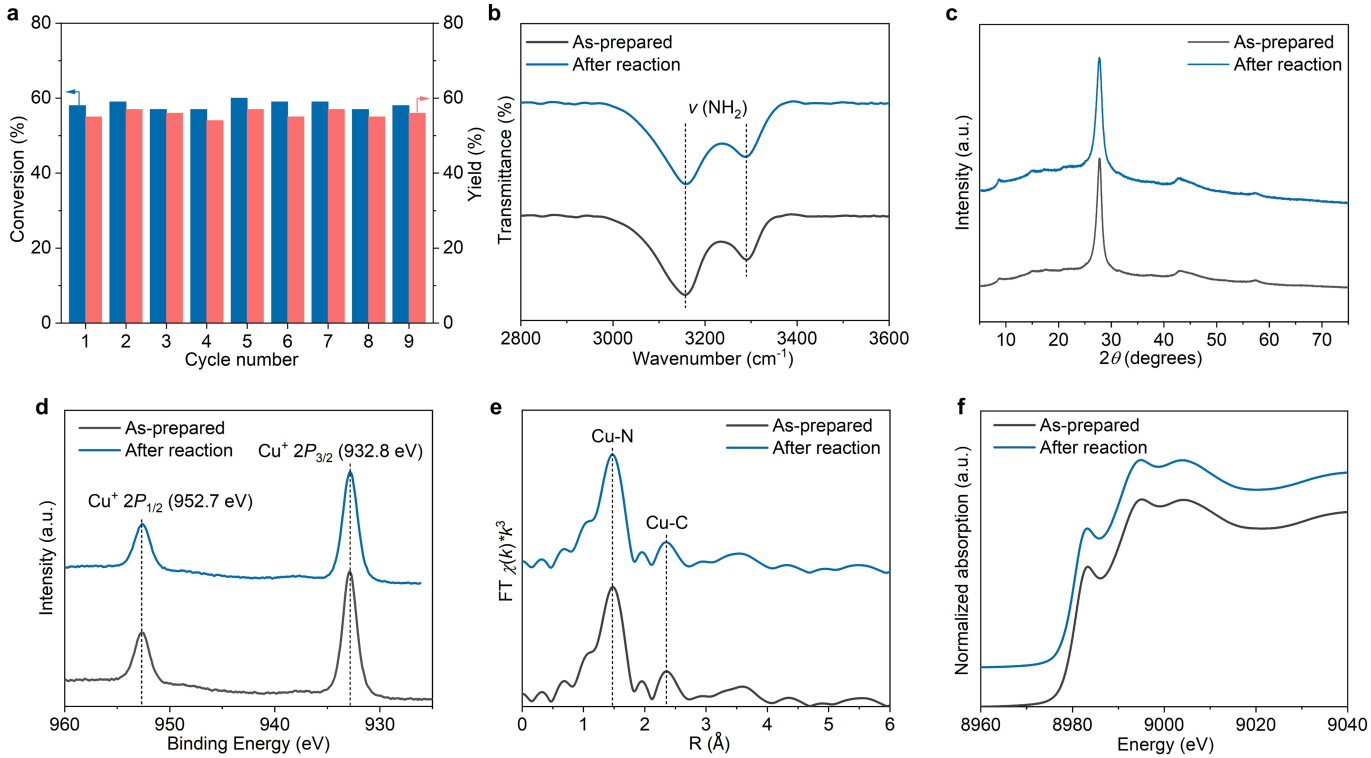

Extended Data Fig. 9 | Stability of Cu_g/PCN in C–O coupling. a, Cycling test for the coupling of 4-iodotoluene with ethanol to form C–O bond over Cu_g/PCN. FTIR spectra (**b**), XRD pattern (**c**), XPS spectra (**d**), Cu K-edge Fourier-transformed EXAFS (**e**) and XANES (**f**) spectra of the as-prepared Cu_g/PCN and the catalyst recovered after nine reaction cycles.